

EIG - II. Intriguing characteristics of the most extremely isolated galaxies

O. Spector* and N. Brosch

*Wise Observatory and the Beverly and Raymond Sackler School of Physics and Astronomy,
Tel Aviv University, Tel Aviv 69978, Israel*

Accepted 2017 March 17. Received 2017 March 17; in original form 2016 March 10

ABSTRACT

We have selected a sample of 41 extremely isolated galaxies (EIGs) from the local universe using both optical and HI ALFALFA redshifts (Spector & Brosch 2016). Narrow band H_{α} and wide band imaging along with public data were used to derive star formation rates (SFRs), star formation histories (SFHs), and morphological classifications for the EIGs. We have found that the extreme isolation of the EIGs does not affect considerably their star-formation compared to field galaxies. EIGs are typically ‘blue cloud’ galaxies that fit the ‘main sequence of star forming galaxies’ and may show asymmetric star formation and strong compact star-forming regions. We discovered surprising environmental dependencies of the HI content, M_{HI} , and of the morphological type of EIGs; The most isolated galaxies (of subsample EIG-1) have lower M_{HI} on average (with 2.5σ confidence) and a higher tendency to be early-types (with 0.94 confidence) compared to the less isolated galaxies of subsample EIG-2. To the best of our knowledge this is the first study that finds an effect in which an isolated sample shows a higher fraction of early-types compared to a less isolated sample. Both early-type and late-type EIGs follow the same colour-to- M_* , SFR-to- M_* (‘main sequence’) and M_{HI} -to- M_* relations. This indicates that the mechanisms and factors governing star formation, colour and the M_{HI} -to- M_* relation are similar in early-type and late-type EIGs, and that the morphological type of EIGs is not governed by their M_{HI} content, colour or SFR.

Key words: galaxies: star formation – galaxies: evolution – galaxies: structure

1 INTRODUCTION

The research described here is part of an extensive study of star formation properties and evolution of galaxies in different environments and of various morphological types, conducted in the past few decades (e.g., Brosch 1983; Almoznino 1995; Almoznino & Brosch 1998; Brosch et al. 1998; Heller 2001; Brosch et al. 2006, 2008; Zitrin & Brosch 2008). Specifically, we studied galaxies in the most extremely underdense regions of the local Universe. These galaxies are particularly interesting since they evolved with little or no environmental interference in the last few Gyr, and are therefore useful for validating and calibrating galaxy evolution models. Furthermore, when compared to galaxies in denser regions, they illuminate the overall effects of the environment on the evolution of galaxies.

It is well-known that extremely dense environments

can greatly influence the star formation (SF) in galaxies. Tidal interactions and mergers of galaxies can trigger extreme starbursts with SFR up to $10^3 M_{\odot} \text{ yr}^{-1}$, while isolated galaxies hardly ever exhibit $\text{SFR} > 20 M_{\odot} \text{ yr}^{-1}$ (Kennicutt 1998). Although the effect on SFR may be extreme during mergers in clusters as well as in pairs and loose groups, the effect on SFR averaged over the whole history of a galaxy may be small (Bergvall et al. 2003; Rieke et al. 2009). In cluster environments, apart from the higher rate of interactions, ram pressure by the intracluster medium strips the galaxies of their gas and, therefore, reduces SF. It has also been suggested that in some cases the ram pressure might increase SF (Gavazzi & Jaffe 1985).

Galaxies in isolated environments are generally considered to be gas-rich, fainter, bluer, of later type, and exhibit higher specific star formation rates (SSFRs; SFRs per unit stellar mass) than galaxies in average density environments (Dressler 1980; Grogin & Geller 1999; Pustilnik et al. 2002; Rojas et al. 2004, 2005; Deng et al. 2012; Kreckel et al. 2012;

* E-mail: odedspec@wise.tau.ac.il

Melnyk et al. 2014; Moorman et al. 2016). Some claim that this is not just an effect of the higher abundance of late-type galaxies, and that the late-type galaxies themselves are fainter in under-dense regions than in average density regions (Varela et al. 2004; Croton et al. 2005; Sorrentino et al. 2006).

Numerous other studies also indicate that the properties of galaxies are influenced by their neighbourhood. Brosch & Shaviv (1982) found that the inner regions of isolated galaxies are bluer, compared to ‘field’ galaxies. This was later suggested to be a consequence of intensive formation of massive stars in the nuclei (Brosch & Isaacman 1982). Varela et al. (2004) found that bars are less frequent in isolated galaxies than in perturbed galaxies. Fernández Lorenzo et al. (2014) found that bluer pseudo-bulges tend to reside in neighbourhoods with a higher probability of tidal perturbation. They suggest that the environment could be playing a role in rejuvenating pseudo-bulges. Wang & White (2012) found that satellite galaxies around isolated bright primary galaxies are systematically redder than field galaxies of the same stellar mass, except around primaries with $\log(M_*/M_\odot) < 10.8$, where the satellites’ colours were similar or even bluer.

This work attempts, among other things, to help resolve the question of ‘Nature vs. Nurture’; does the evolution of galaxies depend only on their content or do their large-scale environments have a significant evolutionary influence. Some argue that galaxy formation is driven predominantly by the mass of the host DM halo, and is nearly independent of the larger-scale halo environment (e.g., Croton & Farrar 2008; Tinker & Conroy 2009). This is supported by their simulation models that produce void galaxies conforming to some observed statistical properties (e.g., colour distribution, luminosity function and nearest neighbour statistics). However, since there are many galaxy properties that most simulations cannot predict (e.g., HI content), and since the halo mass of galaxies cannot be directly measured, this hypothesis is hard to prove or disprove.

We have chosen a sample of extremely isolated galaxies (EIGs) from the local universe based on a simple isolation criterion. The neighbourhood properties of this sample were analysed using both observational data and cosmological simulations. The cosmological simulations were further used to estimate the properties and histories of the dark matter (DM) haloes in which the sample EIGs reside. The sample and its analysis are described in detail in the first paper of this series, Spector & Brosch (2016) (SB16), and are summarized here in Section 2.

Extensive optical observations of the sample EIGs in broad-band and rest-frame H_α were performed using the one meter telescope of the Florence and George Wise Observatory¹ (WO). Section 3 describes these observations and their processing. The results of these observations, along with public observational data, were used to measure the current SFRs and to estimate SFHs. These observational results are described in section 4. Analysis of these results is presented in section 5, and the findings are discussed in section 6.

Throughout this work, unless indicated otherwise, Λ cold dark matter (Λ CDM) cosmology with the seven-year Wilkinson Microwave Anisotropy Probe data (WMAP7, Bennett et al. 2011) parameters are used, including the dimensionless Hubble parameter $h = 0.704$. We adopt here the solar g -band absolute magnitude of $M_{g,\odot} = +5.12$ (according to the Sloan Digital Sky Survey, SDSS, DR7 web site²).

2 THE SAMPLE

We have chosen the sample of EIGs using a simple isolation criterion: a galaxy is considered an EIG and is included in the sample if it has no known neighbours closer than a certain neighbour distance limit in 3D redshift space (200 km s^{-1} or 300 km s^{-1} as explained below) and if its redshift is in the range $2000 < cz < 7000 \text{ km s}^{-1}$. No magnitude, HI mass or size limit was used in the selection of candidate neighbours. The use of such limits would have somewhat reduced the level of isolation of the sample (especially for the closer EIGs) and therefore was not preferred. Not using such limits, however, complicates somewhat the analysis of the sample’s isolation level (described in section 3 of SB16 and summarized below). It also causes the sensitivity limits (listed below) and the isolation level to depend on redshift. Higher redshift EIGs are less isolated on average than lower redshift EIGs. For this reason, the redshift of EIGs was limited to 7000 km s^{-1} .

One of the unique advantages of the EIG sample we study here is that, apart from the optical redshift data commonly used to estimate environment density, it also utilized HI redshifts from the Arecibo Legacy Fast ALFA survey (ALFALFA) survey. The ALFALFA survey is a second-generation untargeted extragalactic HI survey initiated in 2005 (Giovanelli et al. 2005, 2007; Saintonge 2007). This survey utilizes the superior sensitivity and angular resolution of the Arecibo 305 m radio telescope to conduct the deepest ever census of the local HI Universe. ALFALFA was particularly useful in verifying the isolation of the target galaxies, since by being an HI survey it easily measures redshifts of low surface brightness galaxies (LSBs) and other low-luminosity late-type neighbours that are often difficult to detect optically but abound with HI. The ALFALFA dataset we used was the “ $\alpha.40$ HI source catalogue” ($\alpha.40$; Haynes et al. 2011). This catalogue covers 40 percent of the final ALFALFA survey area ($\sim 2800 \text{ deg}^2$) and contains 15855 sources. The sensitivity limit of the ALFALFA dataset is given by eq. (6) and (7) of Haynes et al. (2011) as function of the velocity width of the HI line profile, W_{50} . For a typical value $W_{50} = 100 \text{ km s}^{-1}$ the sensitivity limit of the ALFALFA dataset is $\sim 0.6 \text{ Jy km s}^{-1}$. For the redshift range of the EIG sample this translates to HI mass, $\log(M_{\text{HI}}/M_\odot)$, sensitivity limit of ~ 8.0 (for $cz = 2000 \text{ km s}^{-1}$) to ~ 9.1 (for $cz = 7000 \text{ km s}^{-1}$).

The search criterion was applied to two sky regions, one in the spring sky (Spring) and the other in the autumn sky (Autumn) as described in Table 1. These particular regions

¹ IAU code 097 - <http://wise-obs.tau.ac.il/>

² www.sdss.org/dr7/algorithms/sdssUBVRITransform.html#vega_sun_colors

Table 1. Sample search regions

	α (J2000)	δ (J2000)	cz [km s^{-1}]
Spring	7h30m–16h30m	4° – 16°	2000–7000
Autumn	22h00m–03h00m	24° – 28°	2000–7000

were selected since they are covered by the α .40 ALFALFA catalogue (Haynes et al. 2011). Both regions include mainly high Galactic latitudes. The Spring region is almost fully covered by spectroscopic data in SDSS DR10 (Ahn et al. 2014).

In addition to ALFALFA, the NASA/IPAC Extragalactic Database³ (NED) was also used as a source for coordinates and redshifts in and around the search regions. The NED dataset we used includes data downloaded from NED on November 13, 2012 for object types: galaxies, galaxy clusters, galaxy pairs, galaxy triples, galaxy groups, and QSO. The completeness functions derived in section 3.2 of SB16 indicate that the sensitivity limit of the NED dataset in terms of g magnitude is ~ 18.5 for the Spring sky region and ~ 17 for the Autumn sky region. For the redshift range of the EIG sample this translates to absolute g magnitude sensitivity limit of ~ 13.8 (for $cz = 2000 \text{ km s}^{-1}$) to ~ 16.5 (for $cz = 7000 \text{ km s}^{-1}$) for the Spring sky region, and ~ 15.3 to ~ 18.0 for the Autumn sky region. A rough conversion to stellar mass, M_* , assuming g luminosity to mass ratio as that of the sun, gives a $\log(M_*/M_\odot)$ sensitivity limit of ~ 7.6 (for $cz = 2000 \text{ km s}^{-1}$) to ~ 8.6 (for $cz = 7000 \text{ km s}^{-1}$) for the Spring sky region, and ~ 8.2 to ~ 9.2 for the Autumn sky region.

The EIGs, studied here, were divided to three subsamples:

1. Galaxies that passed the criterion using both NED and ALFALFA data with a neighbour distance limit of 300 km s^{-1} . This translates to not having any known neighbour within a distance of $3 h^{-1} \text{ Mpc} \cong 4.26 \text{ Mpc}$.
2. Galaxies that passed the criterion using NED data with a neighbour distance limit of $3 h^{-1} \text{ Mpc}$, but did not pass using ALFALFA data (had neighbours closer than $3 h^{-1} \text{ Mpc}$ in the ALFALFA database).
3. Galaxies for which the distance to the closest neighbour in NED’s data is $2 - 3 h^{-1} \text{ Mpc}$ (regardless of the distance to the closest neighbour in ALFALFA’s data).

Subsamples 1 and 2 contain all catalogued galaxies that passed their criteria in the studied sky regions. Subsample 3 contains only those galaxies that seemed to be isolated in the various searches performed over the years, but were later found to have neighbours in the range $2 - 3 h^{-1} \text{ Mpc}$ (with the 2012 NED dataset described above). It also contains a galaxy, EIG 3s-06, which was found by searching the ALFALFA data alone, but had neighbours in the range $2 - 3 h^{-1} \text{ Mpc}$ in the NED dataset.

The galaxies were named according to their subsample and sky region, using the following format:

EIG BR-XX

where:

B is the galaxy’s subsample (1, 2 or 3, as described above);
R is the sky region: ‘s’ - Spring, ‘a’ - Autumn;
XX is the serial number of the galaxy in the subsample.

So, for example, object EIG 3s-06 is the sixth galaxy in subsample 3 of the spring sky region.

The galaxies of the different subsamples are listed in Tables 2 through 7 of SB16. Subsample EIG-1 contains 21 galaxies (14 Spring and 7 Autumn galaxies). Subsample EIG-2 contains 11 galaxies (7 Spring and 4 Autumn galaxies). Subsample EIG-3 contains 9 galaxies (7 Spring and 2 Autumn galaxies). In total, the sample contains 41 EIGs. Notes regarding specific EIGs are listed in Appendix A.

The use of the ALFALFA unbiased HI data significantly improved the quality of the sample. Out of 32 galaxies that passed the $3 h^{-1} \text{ Mpc}$ criterion using NED data alone, 11 galaxies did not pass the criterion when tested with ALFALFA data.

Neighbourhood properties of the sample EIGs were analysed using both observational data and cosmological simulations. The analysis based on observational data is described in detail in section 2.4 of SB16. Tables 8 and 9 of SB16 list properties such as the distance to the closest neighbour and neighbour counts for each sample EIG. A comparison to random galaxies show that on average the neighbourhood density of EIGs is about one order of magnitude lower than that of field galaxies. Observational neighbourhood data further indicates that EIGs tend to reside close to walls and filaments rather than in centres of voids.

Using cosmological simulations, we confirmed that the EIG-1 and EIG-2 subsamples are a subset of galaxies significantly more isolated than the general galaxy population. Apart from the low density regions in which they reside, EIGs are characterized by normal mass haloes, which have evolved gradually with little or no major mergers or major mass-loss events. As a result of their low-density environments, the tidal acceleration exerted on EIGs is typically about one order of magnitude lower than the average tidal acceleration exerted on the general population of galaxies. The level of contamination in the sample, i.e. the fraction of EIGs which are not in extremely isolated environments or which experienced strong interactions in the last 3 Gyr, was found to be 5%–10%. The Spring EIGs seem to be more isolated than the Autumn EIGs. For further details about the analysis using cosmological simulations and its results see section 3 of SB16.

For similar purposes, other samples of isolated galaxies were defined and studied in ‘the Analysis of the interstellar Medium of Isolated Galaxies’ (AMIGA) international project (Verley et al. 2007; Fernández Lorenzo et al. 2013), in the ‘Two Micron Isolated Galaxy’ catalogue (2MIG; Karachentseva et al. 2010), in the ‘Local Orphan Galaxies’ catalogue (LOG; Karachentsev et al. 2011, 2013), and in the ‘Void Galaxy Survey’ (VGS; Kreckel et al. 2012). In section 2.5 of SB16 these were discussed and compared to the EIG sample studied here. The comparison showed that the EIG sample galaxies are significantly more isolated than the AMIGA, 2MIG and LOG galaxies (in terms of the distance to the closest neighbour) and that the EIG-1 galaxies are

³ <http://ned.ipac.caltech.edu/>

more isolated than the VGS galaxies. Other notable isolated galaxy samples, not analysed in SB16, are the UNAM-KIAS catalogue of isolated galaxies (Hernández-Toledo et al. 2010) and the catalogues of isolated galaxies, isolated pairs, and isolated triplets in the local Universe of Argudo-Fernández et al. (2015).

3 OBSERVATIONS AND DATA PROCESSING

3.1 Instrumentation

Optical observations were performed using the 1 meter (40 inch) telescope of the WO. The telescope was equipped with a 1300×1340 back-illuminated Princeton Instruments CCD with pixel size of 0.57 ± 0.01 arcsec pixel⁻¹ and an overall field of view of $\sim 12.5'$. EIGs were imaged using wide band Bessell U, B, V, R and I filters and a set of narrow-band rest-frame H $_{\alpha}$ filters for various redshifts. A thorough description of the H $_{\alpha}$ filter set is provided in appendix A of Spector (2015).

3.2 Observations

We observed 34 of the EIGs in the *R* and in one or two appropriate H $_{\alpha}$ narrow bands. Of these EIGs, those not covered by SDSS (and a few that are) were imaged also in the U, B, V and I bands. At least six dithered exposures were obtained in each filter. Exposures were 20 minutes long for the H $_{\alpha}$ and U bands, and 10 minutes long for the B, V, and I bands. Exposures in the *R* band were 5 minutes long for EIGs that were observed only in *R* and H $_{\alpha}$, and 10 minutes long for EIGs observed in all bands. Whenever possible, the exposures of the *R* and H $_{\alpha}$ bands were taken in time proximity so that their atmospheric conditions and air-masses would remain similar. This is important for the accurate measurement of the H $_{\alpha}$ equivalent width (EW), as described in Spector et al. (2012) (S12).

Photometric calibrations of the wide bands were performed for EIGs not covered by SDSS, and for a few that are, using Landolt (1992) standards. Spectrophotometric calibrations of the H $_{\alpha}$ band were performed using Oke (1990) standard stars that have well known spectra, are stable, and have as few features around H $_{\alpha}$ as possible.

Images were processed using the Image Reduction and Analysis Facility (IRAF) software⁴. The reduction pipeline included standard bias subtraction, flat-fielding and image alignment. For images taken in the I band, a fringe removal step was added.

3.3 Net-H $_{\alpha}$ images

Net-H $_{\alpha}$ (nH $_{\alpha}$) data were derived from the measurements using the recipes described in S12. EW values were derived using eq. 12 and 16 of S12. The nH $_{\alpha}$ fluxes were derived using eq. 7 and 12 of S12 after applying the photometric calibrations described in section 3 of S12. Eq. 12, 16 and 7 of SB12 are shown here for reference:

$$\text{cps}_{N,line} \cong \left(\text{cps}_N - \frac{\text{cps}_W}{\text{WNCR}} \right) \times \left[1 - \frac{1}{\text{WNCR}} \cdot \frac{T_{atm,W}(\lambda_{line}) T_W(\lambda_{line})}{T_{atm,N}(\lambda_{line}) T_N(\lambda_{line})} \right]^{-1} \quad (1)$$

$$\text{EW} \cong \frac{\text{cps}_{N,line}}{\text{cps}_N - \text{cps}_{N,line}} \cdot \frac{\int_0^{\infty} T_N(\lambda) d\lambda}{T_N(\lambda_{line})} \quad (2)$$

$$F_{line} \cong \frac{\text{cps}_{N,line}}{T_{atm,N}(\lambda_{line}) T_N(\lambda_{line}) R_{\lambda}(\lambda_{line})} \quad (3)$$

where:

cps $_N$, cps $_W$ are the measured count rates of the narrow-band (N) and wide-band (W) filters (respectively) in instrumental units (typically analogue to digital units per second, ADU s⁻¹);

cps $_{N,line}$ is the line contribution to cps $_N$ (see also eq. 3 of SB12);

WNCR (wide to narrow continuum ratio) is the ratio between the count rate contributed by the continuum in the W band and the count rate contributed by the continuum in the N band (see also eq. 10 of SB12);

T $_N(\lambda)$, T $_W(\lambda)$ are the transmittance functions of the N and W bands, respectively;

T $_{atm,N}(\lambda)$, T $_{atm,W}(\lambda)$ are the atmospheric transmittance as function of wavelength, including effects of weather, elevation and airmass of observation, when the N and W bands (respectively) were imaged;

R $_{\lambda}$ is the responsivity as function of wavelength of the rest of the electro-optical system (i.e. the telescope and sensors, excluding the transmittance effect of the filters) typically in ADU erg⁻¹ cm²;

λ_{line} is the central wavelength of the emission line;

F $_{line}$ is the emission-line's flux.

The WNCR required for (1) was estimated using the method of WNCR-to-colour linear fit suggested in section 6 of S12 (sixth paragraph). The process included selecting a reference wavelength band for each EIG, the first band with a good quality image from the following list: *V*, *I*, *B*, SDSS *g* and SDSS *i*. In the combined images of these *R* and reference bands foreground stars were identified (using their intensity profiles), and their instrumental colours (reference minus *R*) were measured along with that of the EIG.

All nH $_{\alpha}$ measurements were performed on the individual H $_{\alpha}$ images, each paired with an *R* image taken at the closest time and airmass available. For each such pair, the foreground stars were measured in both the *R* and H $_{\alpha}$ images, and their WNCR values were calculated (the *R* to H $_{\alpha}$ cps ratio). A linear relation between WNCR and the uncalibrated colour was fitted to the results of these foreground stars. The WNCR of the pair of H $_{\alpha}$ and *R* images was then calculated using the fit and the EIG's measured uncalibrated colour.

Next, an nH $_{\alpha}$ image was created for each H $_{\alpha}$ and *R* image pair. The sky level, measured around the EIG, was first subtracted from the H $_{\alpha}$ and *R* images. Then, the images were scaled by their exposure time. Finally, the pixel values of the nH $_{\alpha}$ images were calculated using (1).

⁴ <http://iraf.noao.edu/>

3.4 Photometry

Apertures for the photometric measurements of the EIGs were defined as polygons or as elliptical isophotes fitted to the combined R-band images. The polygonal apertures approximately trace the $R = 26 \text{ mag arcsec}^{-2}$ isophote of the EIGs, but exclude foreground Galactic stars and galaxies, projected close to the EIG. This resulted in some reduction in the measured flux from the EIGs, which was significant only for EIG 2s-06 that has a foreground star of magnitude $r = 15.6$ projected close to its centre. Polygonal apertures were also defined for some resolved HII regions and other regions of interest within the EIGs (see figures 1, 2 and 3 below).

Wherever possible, photometric measurements were made using SDSS calibrated images using the same apertures defined for the WO images. The SDSS calibrations were tested by comparing results of seven EIGs that had photometric calibrations performed at the WO as well as SDSS data. The *UBVRI* magnitudes were converted to *ugriz* SDSS magnitudes using the transformation recommended in Table 1 of Jester et al. (2005) for all stars with $R - I < 1.15$. This is the transformation recommended by SDSS for galaxies.⁵ On average, the results were similar to the SDSS calibrated magnitudes. The standard deviation of the difference between the WO calibration (converted to *ugriz*) and the SDSS calibration was 0.05 mag for r and i , 0.07 mag for g , and 0.11 mag for u and z .

Where available, SDSS measurements were used to calibrate the nH_α flux using the method described in section 3 of S12, in which g , r and i are used to estimate the continuum flux at the rest-frame H_α wavelength. This continuum flux estimate is then multiplied by the equivalent width to obtain the nH_α flux.

Thirteen EIGs had both spectrophotometric and SDSS nH_α calibrations. We found random deviations between the results of the two calibrations, which the original uncertainty propagation estimates did not predict. These may be attributed to the inaccuracy introduced by estimating the continuum at H_α using an interpolation of two or three SDSS magnitude measurements (see section 3 of S12). This was compensated for by adding 0.2 relative uncertainty to the SDSS calibrations.

3.5 Absolute magnitudes and luminosities

To calculate the absolute magnitudes and luminosities, the calibrated apparent magnitudes and fluxes were first corrected for foreground Galactic extinction. The Wise Observatory (*UVBRI*) and SDSS magnitudes were corrected using Galactic extinction NED data based on Schlafly & Finkbeiner (2011).

The Galactic extinctions of the H_α fluxes, $A_{\lambda\text{H}_\alpha}$, were estimated using an interpolation between the r and i extinctions. The interpolation was linear in $\ln(A_\lambda)$ vs. λ , since this fits well A_λ of *ugriz* and *UBVRI*.

This work utilizes data from the Galaxy Evolution Explorer mission (GALEX; Martin et al. 2005), the Two Micron All Sky Survey (2MASS; Skrutskie et al. 2006) and

the Wide-field Infrared Survey Explorer (WISE; Wright et al. 2010). The GALEX (*NUV* and *FUV*) and 2MASS (J , H and K_s) Galactic extinctions were calculated using the A_B and A_V of Schlafly & Finkbeiner (2011) and the 2nd column of Table 2 of Yuan et al. (2013), which gives $R_{band} = A_{band} / (A_B - A_V)$ for each band. The Galactic extinction of the WISE $W3$ and $W4$ bands were estimated using the calculated $A(K_s)$ and the values for $A_{12\mu\text{m}}/A_K$ and $A_{22\mu\text{m}}/A_K$ quoted in column 2 of Table 2 of McClure (2009).

Distance estimates, required for calculating absolute magnitudes and fluxes, were based on the local velocity field model of Mould et al. (2000) that includes terms for the influence of the Virgo Cluster, the Great Attractor, and the Shapley Supercluster. As customary in this field (e.g., Fernández Lorenzo et al. 2012; Haynes et al. 2011; Kreckel et al. 2012) uncertainties were not estimated for these distances. At the low redshifts of the EIGs ($z < 0.024$) K-corrections are not significant compared to the uncertainty that they introduce. Therefore, K-corrections were not applied to the measured magnitudes and fluxes. The apparent magnitudes, m , and fluxes, F (after correcting for Galactic extinction) were converted to absolute magnitudes, M , and luminosities, L , using: $M = m - 5 \cdot \log \frac{(1+z)D_m}{10 \text{ pc}}$ and $L = 4\pi D_m^2 (1+z)^2 \cdot F$, where D_m is the distance estimate (comoving transverse distance).

Further details about the observations and data processing can be found in section 5 of Spector (2015).

4 RESULTS

4.1 Apparent magnitudes and fluxes

Table 2 lists the SDSS apparent magnitudes of the 39 EIGs measured as described in section 3.4.⁶ Photometrically calibrated *UBVRI* (Bessell) measurements were made for eight of the EIGs. Their apparent magnitudes are listed in Table 3.

The combined R and Net- H_α (nH_α) images are shown in figures 1, 2 and 3 (in negative).⁷ Each row of images in the figures relates to a different EIG. The name of the EIG is given on the leftmost image, which shows the combined R image. The second image from the left shows the same R image using a logarithmic scale ($\log R$). The third image from the left shows the combined nH_α image. The rightmost image shows the EIG in false colour; R in orange, and nH_α in azure (both using a negative linear scale). The upper bar in the rightmost image shows the physical scale calculated using the distance estimate described in section 3.5. The lower bar in the rightmost image shows the angular size scale.

⁶ Two of the EIGs, 1a-05 and 1a-06, are not in the SDSS footprint and were not imaged in the WO.

⁷ The images of EIG 2s-04 are not shown due to a bright foreground star that does not allow to clearly identify it in the image (see details in Appendix A).

⁵ <http://www.sdss3.org/dr9/algorithms/sdssUBVRITransform.php>

Table 2. Apparent SDSS magnitudes

EIG	<i>u</i>	<i>g</i>	<i>r</i>	<i>i</i>	<i>z</i>
1s-01	17.37 ± 0.03	16.633 ± 0.007	16.315 ± 0.007	16.090 ± 0.008	15.99 ± 0.03
1s-02	16.766 ± 0.008	15.911 ± 0.003	15.552 ± 0.003	15.378 ± 0.003	15.243 ± 0.006
1s-03	17.29 ± 0.03	16.200 ± 0.007	15.61 ± 0.01	15.231 ± 0.008	14.99 ± 0.02
1s-04	18.43 ± 0.05	17.47 ± 0.01	17.09 ± 0.01	16.87 ± 0.01	16.90 ± 0.05
1s-05 ^a	—	—	—	—	—
1s-06	—	16.719 ± 0.006	16.360 ± 0.007	16.14 ± 0.01	15.87 ± 0.03
1s-07	—	17.482 ± 0.006	17.005 ± 0.005	16.698 ± 0.006	16.50 ± 0.02
1s-08	18.86 ± 0.03	17.839 ± 0.007	17.416 ± 0.007	17.247 ± 0.008	16.81 ± 0.02
1s-09	—	16.900 ± 0.005	16.679 ± 0.006	16.518 ± 0.007	16.50 ± 0.02
1s-10	18.20 ± 0.02	17.480 ± 0.005	17.273 ± 0.007	17.17 ± 0.01	17.06 ± 0.02
1s-11	—	16.37 ± 0.09	15.81 ± 0.01	15.6 ± 0.1	15.35 ± 0.08
1s-12	18.77 ± 0.02	17.904 ± 0.006	17.689 ± 0.007	17.51 ± 0.01	17.53 ± 0.03
1s-13	18.99 ± 0.09	17.92 ± 0.02	17.69 ± 0.02	17.59 ± 0.03	17.74 ± 0.07
1s-14 ^b	17.0 ± 0.1	15.7 ± 0.1	15.1 ± 0.1	14.8 ± 0.1	14.6 ± 0.1
1a-01	16.79 ± 0.02	15.686 ± 0.004	15.194 ± 0.004	14.931 ± 0.004	14.72 ± 0.01
1a-02	18.05 ± 0.03	16.988 ± 0.006	16.464 ± 0.005	16.212 ± 0.006	16.08 ± 0.02
1a-03	—	17.50 ± 0.02	17.0 ± 0.2	16.91 ± 0.06	16.7 ± 0.1
1a-04 ^c	15.40 ± 0.06	13.49 ± 0.02	12.62 ± 0.03	12.13 ± 0.03	11.72 ± 0.03
1a-07	17.56 ± 0.02	16.649 ± 0.004	16.327 ± 0.005	16.138 ± 0.005	15.99 ± 0.02
2s-01	18.45 ± 0.04	17.64 ± 0.01	17.35 ± 0.01	17.13 ± 0.02	16.96 ± 0.05
2s-02	18.23 ± 0.05	17.084 ± 0.008	16.591 ± 0.009	16.34 ± 0.01	16.34 ± 0.03
2s-04	—	18.20 ± 0.02	17.86 ± 0.02	17.52 ± 0.02	17.5 ± 0.1
2s-05	16.53 ± 0.01	15.562 ± 0.003	15.118 ± 0.003	14.908 ± 0.003	14.738 ± 0.008
2s-06 ^d	17.5 ± 0.2	16.5 ± 0.2	16.1 ± 0.2	15.8 ± 0.2	15.7 ± 0.2
2s-07	18.13 ± 0.02	16.926 ± 0.005	16.476 ± 0.004	16.268 ± 0.005	16.10 ± 0.01
2s-08	18.04 ± 0.02	17.450 ± 0.005	17.435 ± 0.006	17.606 ± 0.008	17.48 ± 0.02
2a-01	17.05 ± 0.03	15.642 ± 0.004	14.794 ± 0.003	14.319 ± 0.004	13.94 ± 0.01
2a-02	17.90 ± 0.08	16.73 ± 0.01	16.09 ± 0.01	15.74 ± 0.01	15.46 ± 0.03
2a-03	16.99 ± 0.02	15.906 ± 0.003	15.441 ± 0.003	15.179 ± 0.004	15.00 ± 0.01
2a-04	19.3 ± 0.2	17.85 ± 0.03	17.43 ± 0.02	17.20 ± 0.04	16.94 ± 0.09
3s-01	18.47 ± 0.06	17.59 ± 0.02	17.15 ± 0.02	16.89 ± 0.02	16.82 ± 0.08
3s-02	—	17.134 ± 0.008	16.84 ± 0.01	16.67 ± 0.01	16.55 ± 0.04
3s-03	16.97 ± 0.01	16.136 ± 0.004	15.832 ± 0.004	15.713 ± 0.005	15.58 ± 0.01
3s-04	—	19.03 ± 0.02	18.77 ± 0.03	18.82 ± 0.04	18.9 ± 0.1
3s-05	—	16.305 ± 0.006	15.805 ± 0.006	15.573 ± 0.007	15.37 ± 0.02
3s-06	—	17.422 ± 0.009	17.03 ± 0.01	16.88 ± 0.01	16.65 ± 0.03
3s-07	—	17.318 ± 0.007	16.891 ± 0.007	16.618 ± 0.009	16.51 ± 0.03
3a-01	16.41 ± 0.02	15.466 ± 0.004	15.138 ± 0.004	14.944 ± 0.004	14.62 ± 0.02
3a-02	17.36 ± 0.03	16.126 ± 0.004	15.468 ± 0.004	15.075 ± 0.004	14.772 ± 0.009

^a No optical counterpart was found for EIG 1s-05 (an ALFALFA object).

^b EIG 1s-14 is projected close to a foreground bright star. Uncertainties were estimated to be 0.1 *mag*.

^c Converted from Landolt (*UBVRI*) magnitudes.

^d EIG 2s-06 has a significant foreground star in front of it. Uncertainties were estimated to be 0.2 *mag*.

Table 3. Apparent *UBVRI* magnitudes

EIG	<i>U</i>	<i>B</i>	<i>V</i>	<i>R</i>	<i>I</i>
1s-10	17.48 ± 0.03	17.91 ± 0.01	17.448 ± 0.007	17.155 ± 0.006	16.81 ± 0.01
1s-11	16.66 ± 0.09	16.74 ± 0.02	16.02 ± 0.02	15.63 ± 0.03	15.19 ± 0.04
1a-04	14.65 ± 0.01	14.041 ± 0.003	12.963 ± 0.002	12.359 ± 0.004	11.596 ± 0.004
2a-01	16.43 ± 0.02	16.11 ± 0.01	15.106 ± 0.003	14.471 ± 0.005	13.704 ± 0.004
2a-02	17.01 ± 0.08	17.14 ± 0.01	16.33 ± 0.01	15.79 ± 0.01	15.21 ± 0.01
3s-03	16.16 ± 0.03	16.48 ± 0.01	16.04 ± 0.02	15.57 ± 0.01	15.19 ± 0.03
3a-01	15.56 ± 0.03	15.796 ± 0.007	15.264 ± 0.006	14.91 ± 0.01	14.516 ± 0.006
3a-02	16.52 ± 0.05	16.52 ± 0.02	15.694 ± 0.007	15.165 ± 0.007	14.520 ± 0.007

Table 4. Morphological classification of the EIGs

Type	EIGs
Late	1s-03, 1s-04, 1s-06, 1s-07, 1s-11, 1s-13, 1s-14, 1a-03, 2s-01, 2s-02, 2s-05, 2s-08, 2a-01, 2a-02, 3s-02, 3s-05, 3s-06, 3s-07, 3a-01, 3a-02
Unknown	1s-01, 1s-08, 1s-10, 2s-07, 3s-03, 3s-04
Early	1s-02, 1s-09, 1s-12, 1a-04, 3s-01

Regions of interest within some of the EIGs were measured individually. The polygonal apertures used for these measurements are drawn (along with their names) on the rightmost images of figures 1, 2 and 3. Observational results of these regions of interest are described in section 4.2. Remarks for specific EIGs are listed in Appendix A.

In Figure 4 the R surface brightness, μ_R , is plotted as function of the distance from the galactic centre, r . The surface brightness was measured on a set of ellipses with different semi-major axes, fitted to each EIG. The μ_R of the innermost $2''$ of each galaxy is not shown to avoid confusion due to point spread function (PSF) effects. μ_R measurements with uncertainty ≥ 0.5 mag arcsec $^{-2}$ are also not shown. Two profiles were fitted for each EIG's μ_R measurements, one typical of a late type galaxy disc (blue dashed line) and the other representing an early-type elliptical galaxy (red solid curve). The disc profile has a Sérsic's index $n = 1$, and was fitted to the outskirts of the galaxy (from half of the maximum r shown in the figure and further). The elliptical profile is a de Vaucouleurs relation, i.e. a Sérsic's index $n = 4$. It was fitted to all the measured points shown in the figure.

The EIGs were classified as early-types or late-types by visual inspection of the images of the EIGs, and the μ_R profiles of Figure 4. Whenever the combination of the images and μ_R profiles did not yield a clear identification, the EIG was classified as 'unknown'. Six out of 31 EIGs (19 per cent) were classified as 'unknown'. We chose to classify such a large fraction as 'unknown' in order to reduce the probability of false identification to a minimum. The morphological types of EIGs 1s-05, 2s-04 and 2s-06 were not classified. EIG 1s-05 was not classified because it cannot be identified in optical images, and EIGs 2s-04 and 2s-06 were not classified because of bright foreground stars projected close to them (see details in Appendix A). The morphological classifications are listed in Table 4.

Ultraviolet data were downloaded from the GALEX (Martin et al. 2005) GR6/7 data release⁸. The available apparent magnitudes of EIGs in the GALEX far-ultraviolet band (m_{FUV}) and near-ultraviolet band (m_{NUV}) are listed in Table 5.

2MASS (Skrutskie et al. 2006) and WISE (Wright et al. 2010) data were downloaded from the NASA/IPAC Infrared Science Archive (IRSA)⁹. The 2MASS data were taken from the All-Sky data release. Thirteen EIGs were identified in its Extended Source Catalogue. For two of these (EIGs 1a-01 and 2a-02) the quoted J , H and K_s magnitudes were not used since they translate to flux suspiciously lower than that

Table 5. GALEX apparent magnitudes

EIG	m_{FUV}	m_{NUV}
1s-01	18.67 ± 0.08	18.54 ± 0.05
1s-03	19.50 ± 0.03	18.88 ± 0.02
1s-04	19.53 ± 0.05	19.06 ± 0.03
1s-06	18.70 ± 0.02	18.41 ± 0.01
1s-07	20.0 ± 0.2	19.72 ± 0.02
1s-08	20.4 ± 0.2	19.84 ± 0.03
1s-10	18.9 ± 0.1	18.63 ± 0.02
1s-11	23.0 ± 0.4	19.77 ± 0.06
1s-12	19.4 ± 0.2	19.36 ± 0.02
1s-13	19.72 ± 0.05	19.43 ± 0.03
1a-01	18.30 ± 0.08	18.07 ± 0.05
1a-02	19.73 ± 0.09	19.26 ± 0.05
1a-03	21.6 ± 0.4	19.6 ± 0.1
1a-04	21.5 ± 0.3	19.35 ± 0.09
1a-06	20.9 ± 0.1	21.1 ± 0.1
1a-07	18.89 ± 0.09	18.58 ± 0.05
2s-01	19.2 ± 0.1	18.93 ± 0.08
2s-02	18.75 ± 0.08	18.36 ± 0.06
2s-05	17.63 ± 0.07	17.27 ± 0.04
2s-07	19.6 ± 0.2	19.5 ± 0.1
2s-08	18.86 ± 0.03	18.59 ± 0.02
2a-01	20.8 ± 0.2	19.30 ± 0.07
2a-03	—	18.11 ± 0.04
2a-04	20.53 ± 0.07	20.18 ± 0.05
3s-02	19.02 ± 0.03	18.73 ± 0.02
3s-03	18.13 ± 0.07	17.72 ± 0.03
3s-04	20.1 ± 0.2	19.89 ± 0.08
3s-05	18.9 ± 0.1	18.45 ± 0.06
3s-06	20.0 ± 0.3	19.31 ± 0.03
3s-07	19.49 ± 0.04	19.05 ± 0.03
3a-01	17.69 ± 0.05	17.27 ± 0.03

Table 6. 2MASS apparent magnitudes

EIG	J	H	K_s
1s-02	14.27 ± 0.07	13.7 ± 0.1	13.5 ± 0.1
1s-03	13.76 ± 0.09	12.63 ± 0.07	12.9 ± 0.2
1a-02	15.1 ± 0.2	14.4 ± 0.2	14.1 ± 0.2
1a-04	10.60 ± 0.02	9.87 ± 0.02	9.52 ± 0.03
1a-05	13.83 ± 0.07	13.3 ± 0.1	13.0 ± 0.1
2s-05	14.11 ± 0.08	13.08 ± 0.08	13.2 ± 0.2
2a-01	12.31 ± 0.04	11.58 ± 0.04	11.18 ± 0.05
2a-03	13.99 ± 0.09	13.8 ± 0.2	13.1 ± 0.2
3s-03	14.6 ± 0.2	13.7 ± 0.2	13.3 ± 0.2
3a-01	14.2 ± 0.1	13.4 ± 0.1	13.7 ± 0.2
3a-02	13.26 ± 0.05	12.79 ± 0.07	12.5 ± 0.1

of the i band. The J , H and K_s apparent magnitudes of the remaining eleven EIGs are listed in Table 6.

WISE data taken from the All-WISE catalogue are listed in Table 8. These include apparent magnitudes in the $W3$ and $W4$ bands (columns m_{W3} and m_{W4} respectively). For some of the EIGs these are measurements through elliptical apertures based on the 2MASS K_s isophotal apertures. Data for EIGs, for which the elliptical aperture mea-

⁸ <http://galex.stsci.edu/GR6/>

⁹ <http://irsa.ipac.caltech.edu>

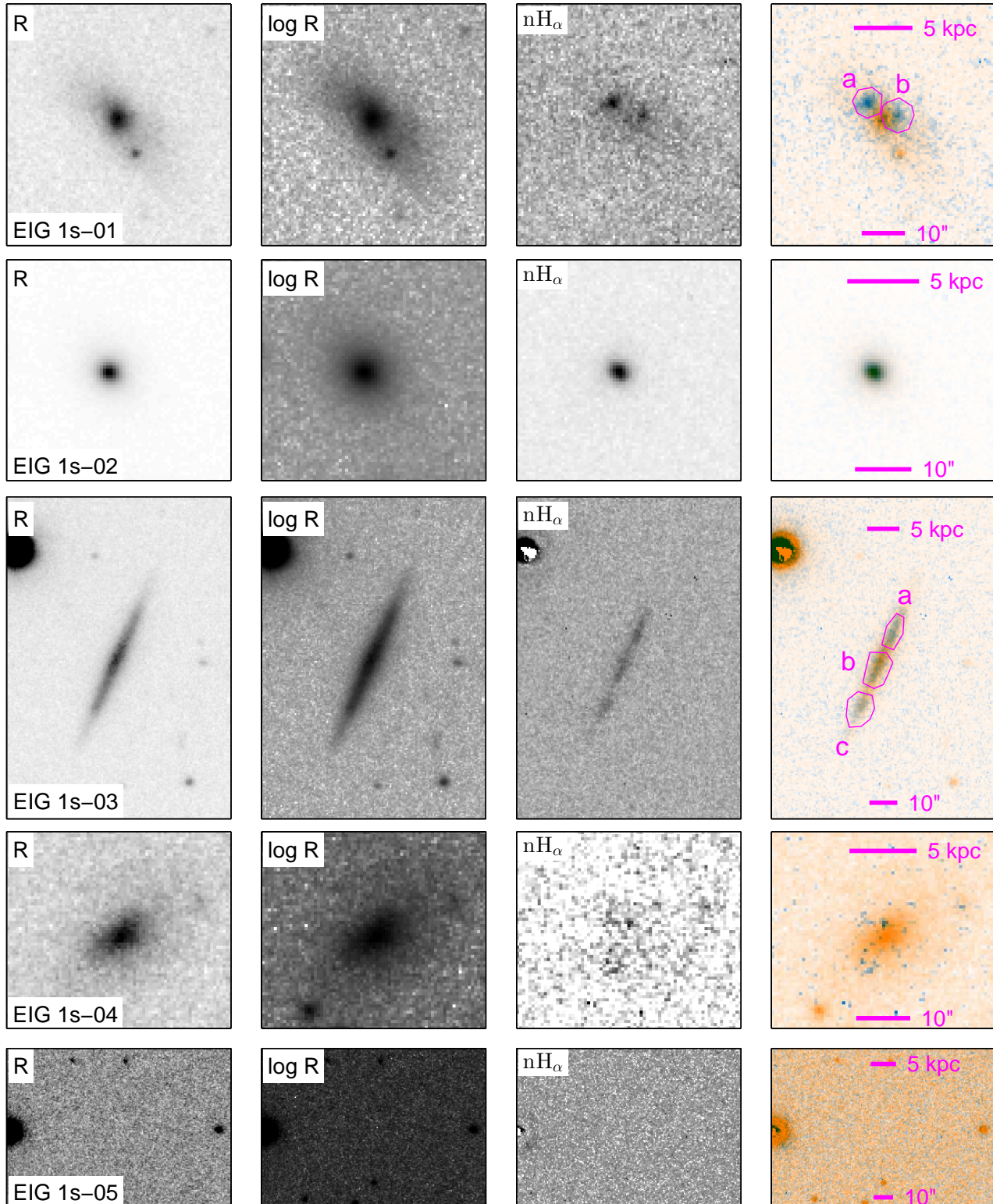


Figure 1. R and nH $_{\alpha}$ images of the EIG-1 subsample (each EIG in a separate row). The columns from left to right show negative images of: the combined R image (in linear scale), the combined R image in logarithmic scale, the combined nH $_{\alpha}$ image (linear scale), the EIG in false colour; R in orange and nH $_{\alpha}$ in azure (linear scale). The rightmost column also includes a physical distance scale, an angular size scale and where applicable the regions of interest measured individually (along with their names).

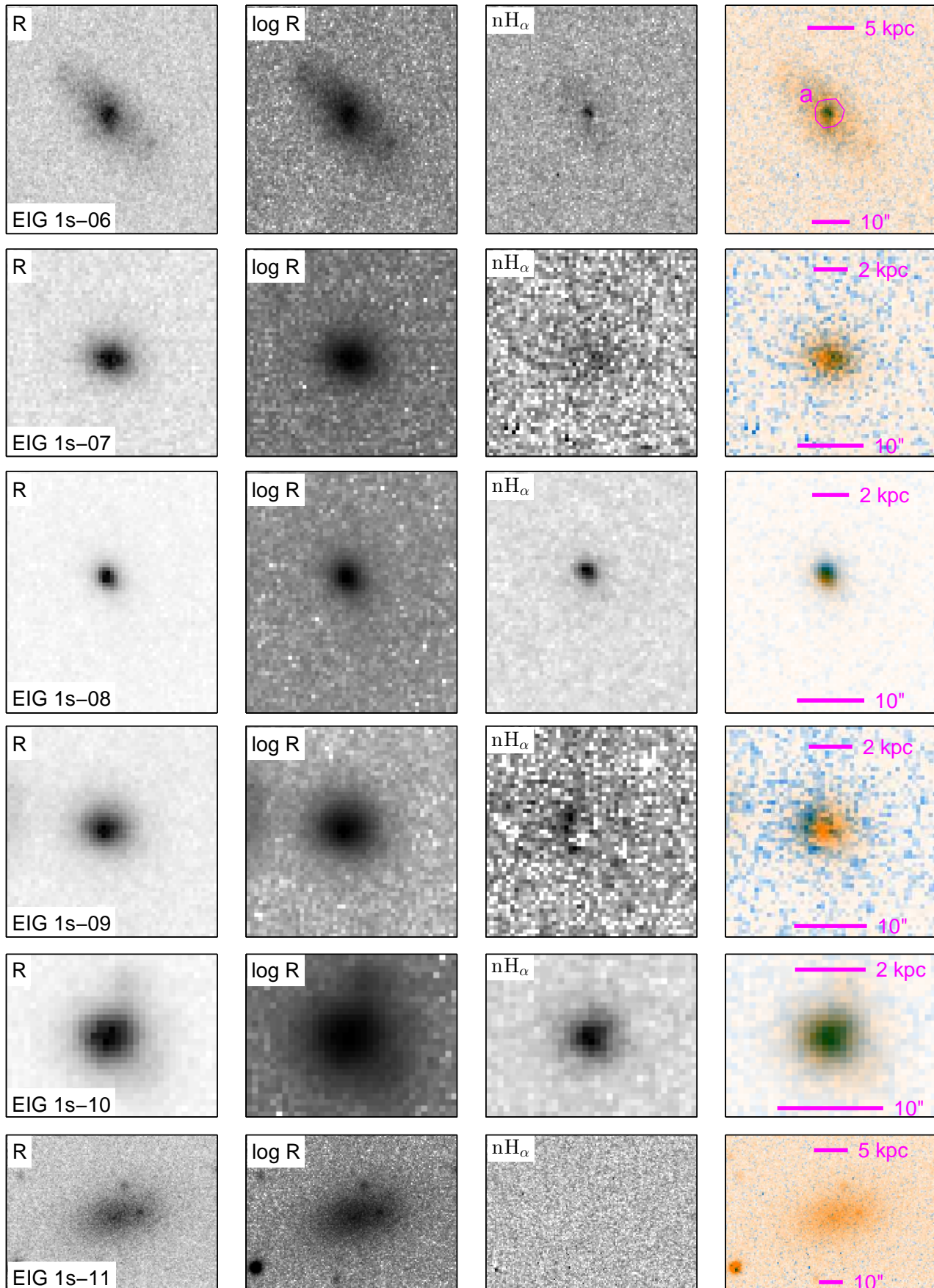


Figure 1 – continued

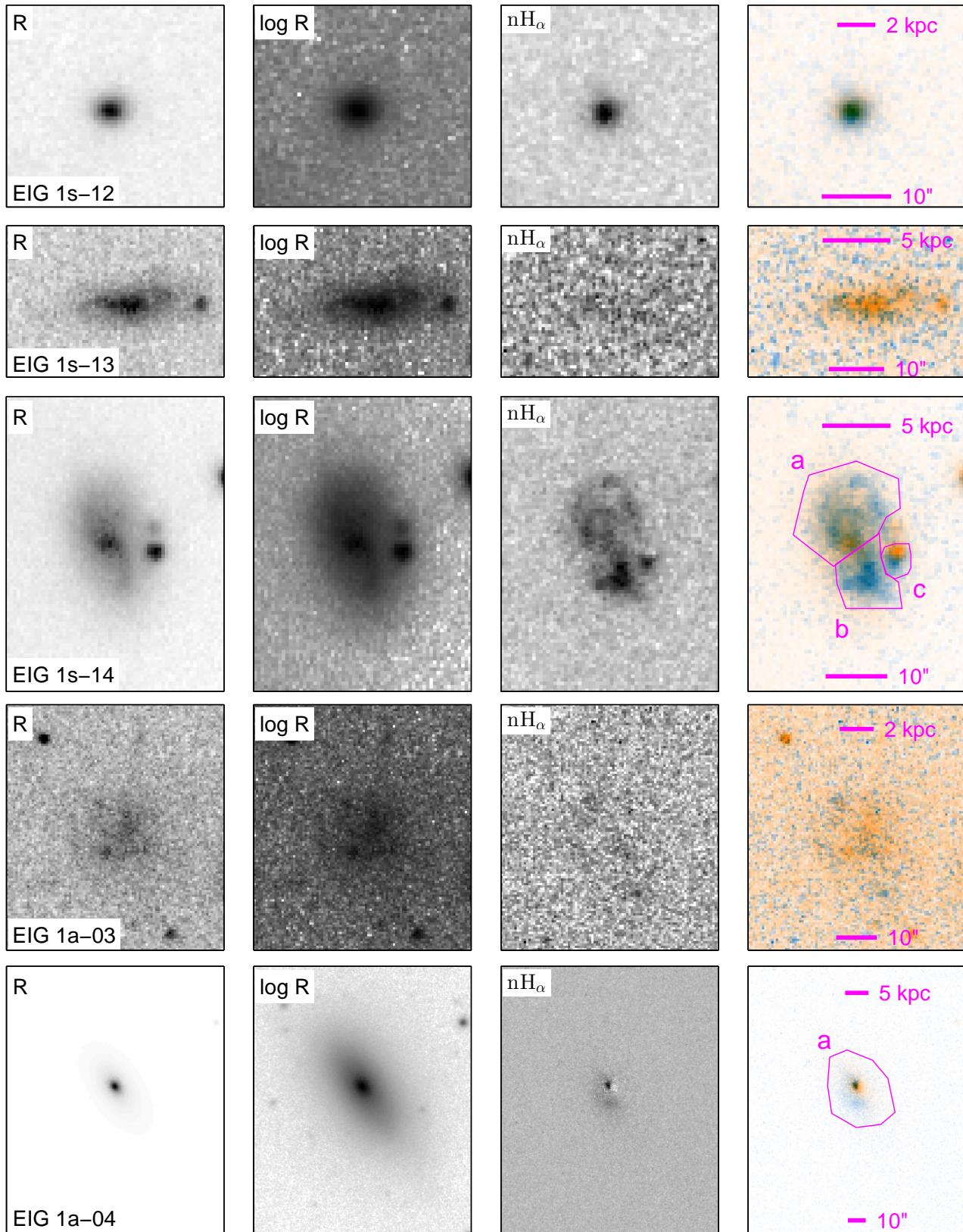


Figure 1 – continued

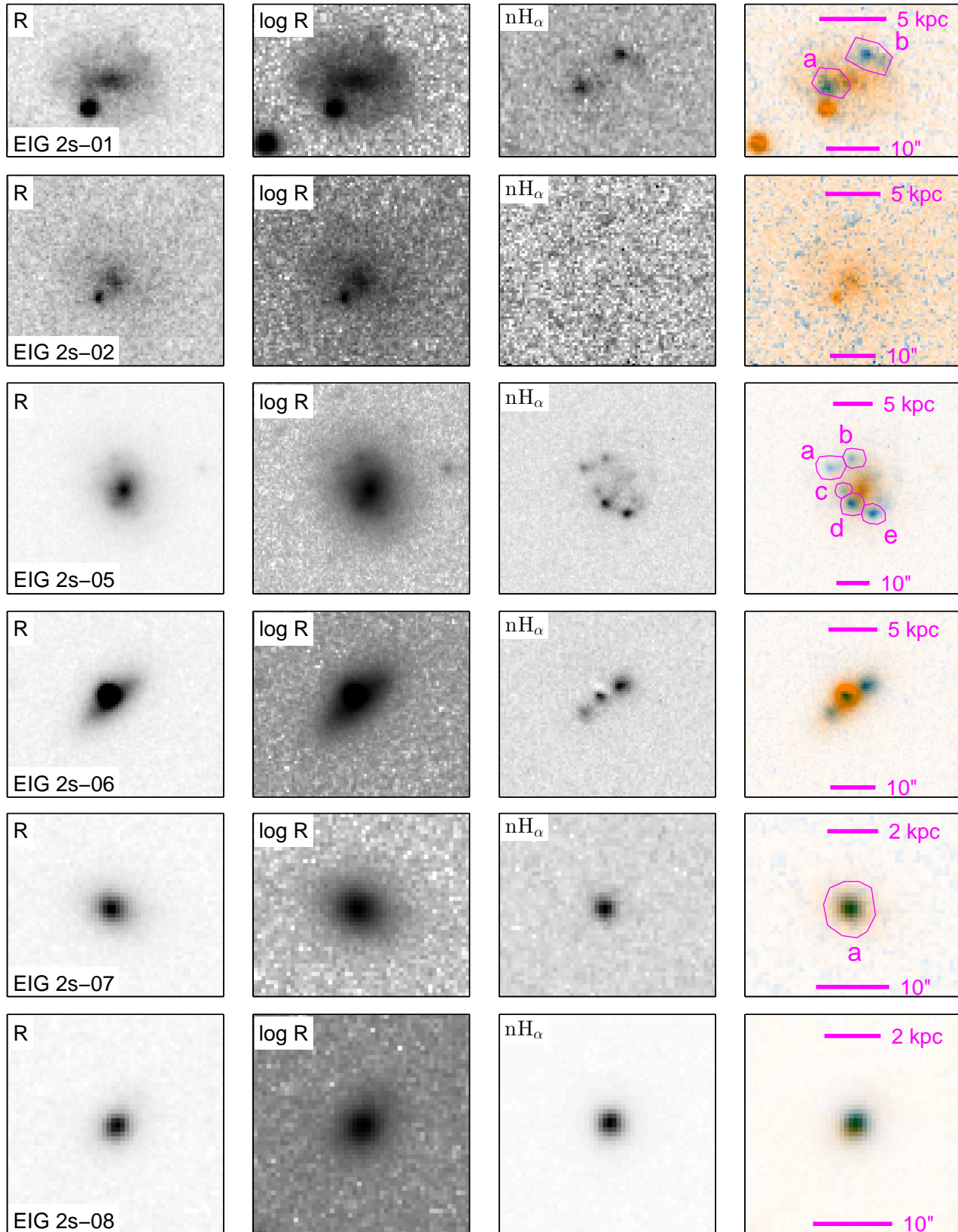


Figure 2. R and nH $_{\alpha}$ images of the EIG-2 subsample (each EIG in a separate row). The columns from left to right show negative images of: the combined R image (in linear scale), the combined R image in logarithmic scale, the combined nH $_{\alpha}$ image (linear scale), the EIG in false colour; R in orange and nH $_{\alpha}$ in azure (linear scale). The rightmost column also includes a physical distance scale, an angular size scale and where applicable the regions of interest measured individually (along with their names).

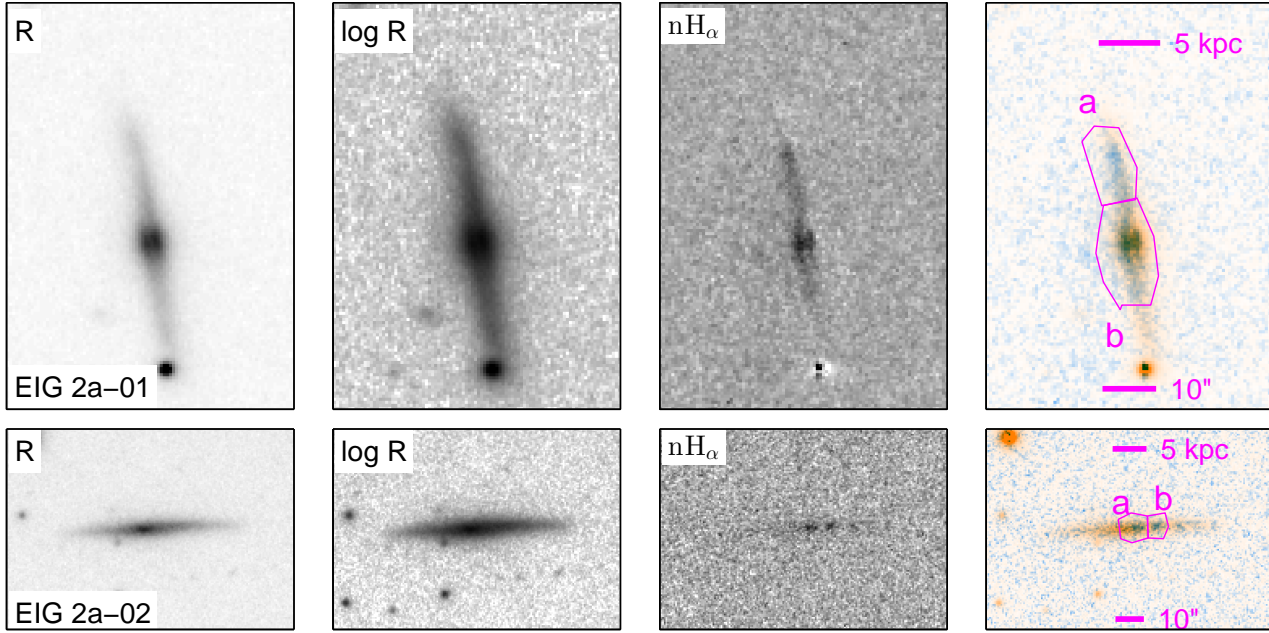


Figure 2 – continued

measurements were not possible, are profile-fitting photometry measurements, or for low SNR measurements the 0.95 confidence magnitude lower limits.

The WISE profile-fitting photometry measurements are less accurate for extended objects than the elliptical aperture measurements. To estimate their uncertainty, a comparison was made between profile-fitting photometry magnitudes and elliptical aperture based magnitudes for eight EIGs for which both were available. On average, the profile-fitting magnitudes were found to be 0.08 ± 0.03 mag (*W3*) and 0.1 ± 0.1 mag (*W4*) lower than the elliptical aperture magnitudes. The standard deviation of the difference between the two measurement methods was found to be ~ 0.3 mag for *W3* and ~ 0.4 mag for *W4*. These standard deviations were added to the estimated uncertainties of the profile-fitting photometry magnitudes.

Table 7 lists data from the ALFALFA $\alpha.40$ catalogue (Haynes et al. 2011). For each EIG that was detected by ALFALFA the velocity width of the HI line profile, W_{50} , corrected for instrumental broadening but not for disc inclination is listed. This is followed by the total HI line flux, F_{HI} , the estimated signal to noise ratio of the detection, SNR, and the HI mass content, M_{HI} . Finally, the category of the HI detection, Code, is listed. Code 1 refers to a source of SNR and general qualities that make it a reliable detection. Code 2 refers to a source with $\text{SNR} \lesssim 6.5$ that does not qualify for code 1 but was matched with a counterpart with a consistent optical redshift, and is very likely to be real.

4.2 Star formation rate

SFRs of the EIGs were calculated using the WO H_α measurements and the WISE *W3* and *W4* measurements. First, the H_α flux and the WISE *W3* and *W4* apparent magnitudes were corrected for Galactic extinction as described in section 3.5 (the corrections for WISE were quite small, up

to 0.018 mag in *W3*, and up to 0.013 mag in *W4*). Then, the *W3* and *W4* Galactic corrected magnitudes were converted to fluxes using the procedure described in section IV.4.h.i.1 of Cutri et al. (2013) for a constant power-law spectra (same as the method used by Wen et al. 2014). The H_α , *W3* and *W4* fluxes were then converted to luminosities ($L_{H_\alpha,obs}$, L_ν ($12 \mu\text{m}$) and L_ν ($22 \mu\text{m}$) respectively) as described in section 3.5.

Wen et al. (2014) found that dust extinction-corrected H_α flux, $L_{H_\alpha,corr}$, can be accurately derived from the observed H_α flux and either the *W3* or *W4* bands using:

$$\begin{aligned} L_{H_\alpha,corr} &= L_{H_\alpha,obs} + 0.038 \cdot \nu L_\nu (12 \mu\text{m}) \\ L_{H_\alpha,corr} &= L_{H_\alpha,obs} + 0.035 \cdot \nu L_\nu (22 \mu\text{m}) \end{aligned} \quad (4)$$

These relations are independent of the metallicity. The relation that uses L_ν ($12 \mu\text{m}$) was found to be slightly more accurate.

The corrected H_α luminosity, $L_{H_\alpha,corr}$, was calculated using equation (4) for both *W3* and *W4*, and the average of the two results was used. If for one of the bands only a lower limit to the magnitude was given, the result of the other band was used. If both bands had only lower limits to their magnitudes, the nominal SFR was calculated assuming zero IR dust emission (i.e., with L_ν ($12 \mu\text{m}$) = L_ν ($22 \mu\text{m}$) = 0) and the effect of the possible IR dust emission was added to the uncertainty of the measurement ($L_{H_\alpha,corr}$ was calculated using both options of (4) with uncertainties in L_ν calculated using the 0.95 confidence lower limit of the *W3* and *W4* fluxes, and the option with the lower uncertainty was used).

Finally, the dust-extinction-corrected H_α luminosity, $L_{H_\alpha,corr}$, was used to calculate the SFR using the following equation adapted from Kennicutt & Evans (2012), Murphy et al. (2011) and Hao et al. (2011):

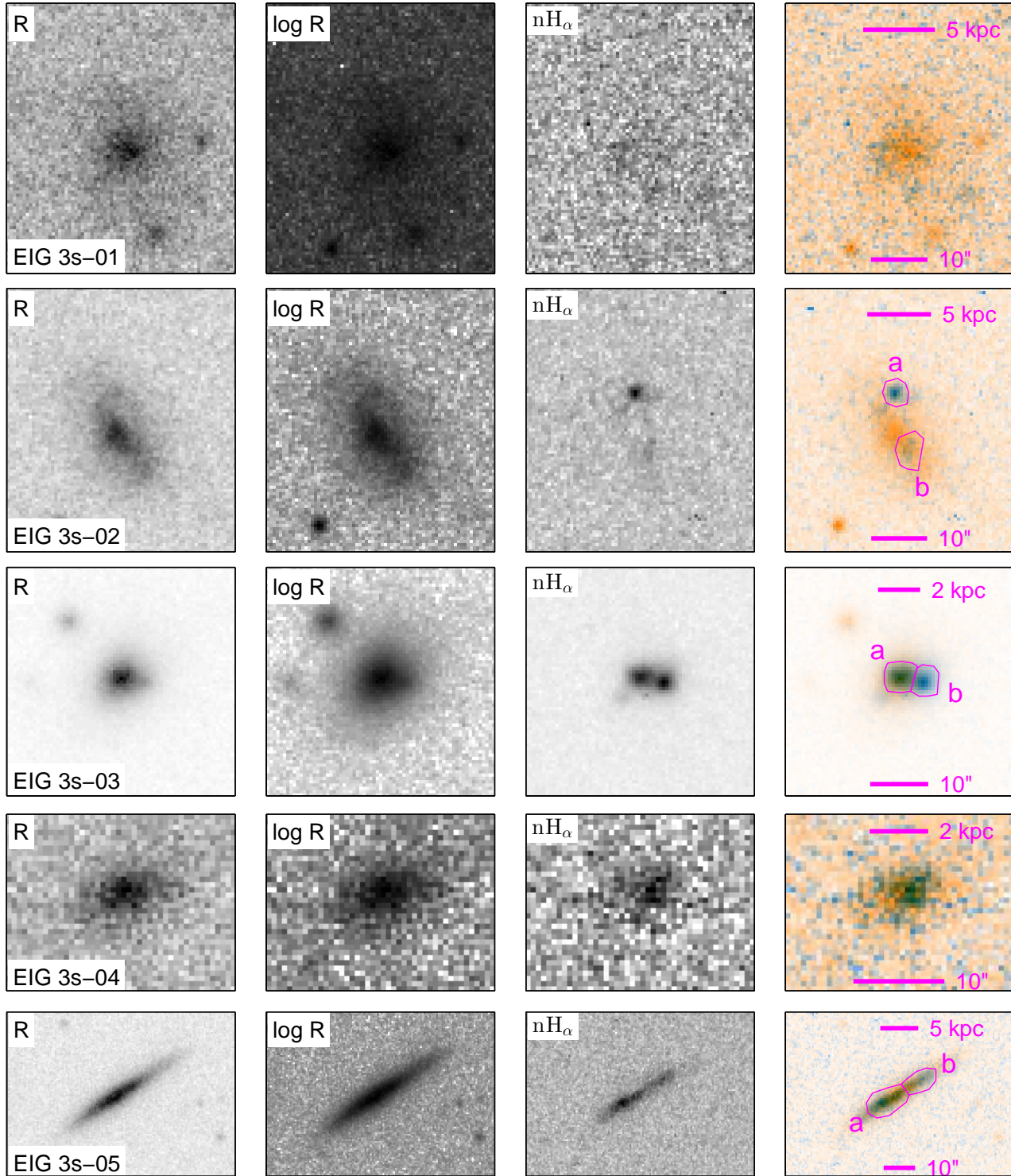
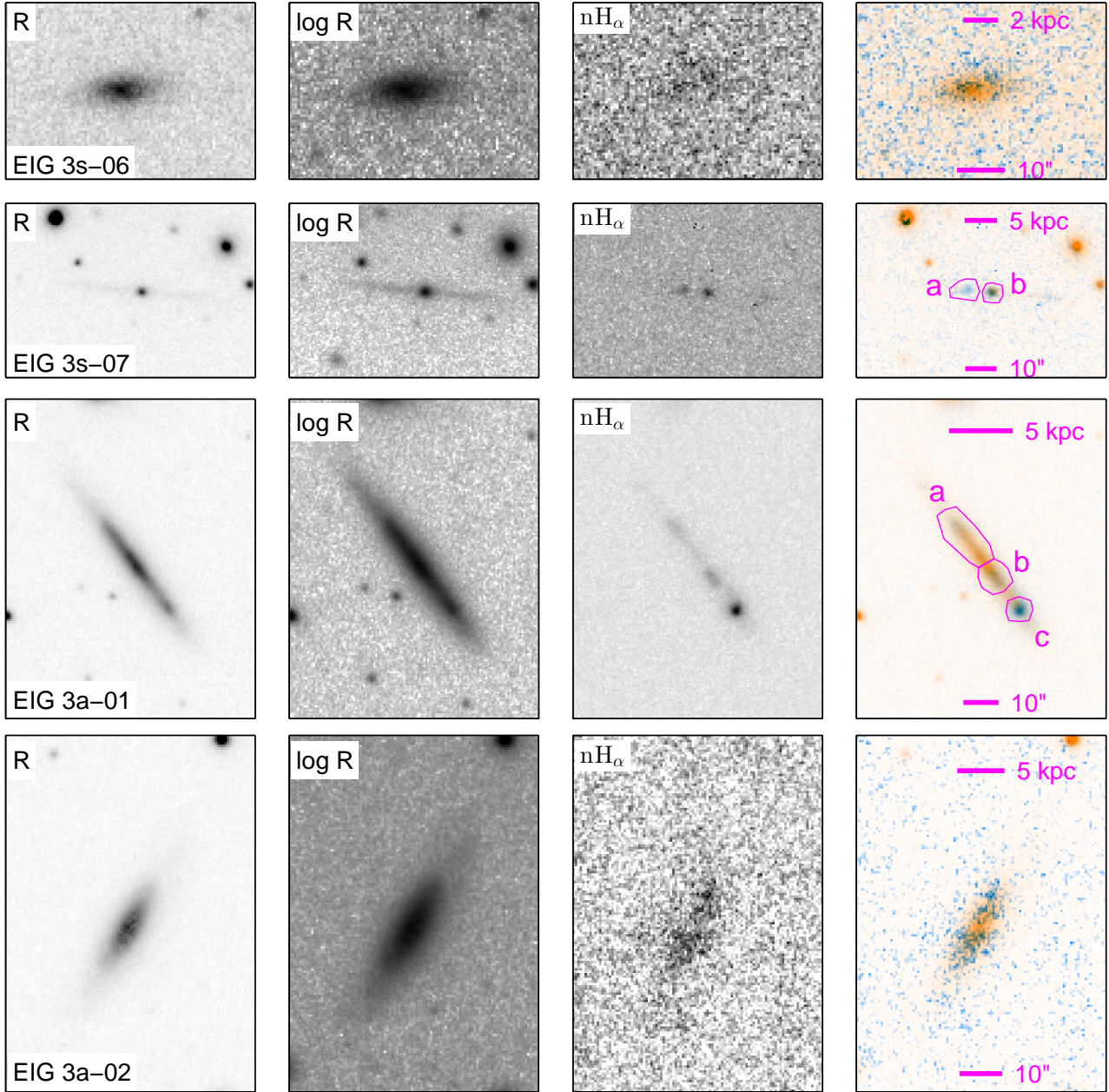


Figure 3. R and nH $_{\alpha}$ images of the EIG-3 subsample (each EIG in a separate row). The columns from left to right show negative images of: the combined R image (in linear scale), the combined R image in logarithmic scale, the combined nH $_{\alpha}$ image (linear scale), the EIG in false colour; R in orange and nH $_{\alpha}$ in azure (linear scale). The rightmost column also includes a physical distance scale, an angular size scale and where applicable the regions of interest measured individually (along with their names).

Figure 3 – *continued*

$$\log \frac{SFR}{M_{\odot} \text{ yr}^{-1}} = L_{H\alpha, \text{corr}} - 41.27 \quad (5)$$

Table 8 lists measured star formation properties of the sample galaxies. For each EIG, the equivalent width, EW, and the H α flux, $F_{H\alpha}$, are listed. These are followed by the WISE magnitudes, m_{W3} and m_{W4} , used for calculating the H α flux that was extinguished within the EIG. Listed finally, are the fraction of the total H α flux extinguished within the EIG, $\text{frac}_{H\alpha, \text{ext}}$, and the SFR.

The H α flux and EW were measured for each region of interest within the EIGs (plotted in figures 1, 2 and 3).

Table 9 lists for each region the H α flux as a fraction of the total EIGs H α flux. Table 10 lists the EWs of the regions.

The regions of interest were defined with some additional area around the star-forming regions so that all the H α flux will be measured. Therefore, the EWs of star-forming regions may be larger than those listed in the Table 10. Similarly, the H α flux fractions of the star-forming regions may be smaller than those listed in Table 9, since some diffuse H α flux from the surrounding area may have been included in the measurement.

As can be seen, the H α flux fractions of the distinct star-forming regions of EIGs do not account for the entire H α flux. In most EIGs the diffuse H α is a significant component. In many of the EIGs (e.g., 1S-13) there are no detectable star-forming regions at all. In some of these the diffused H α

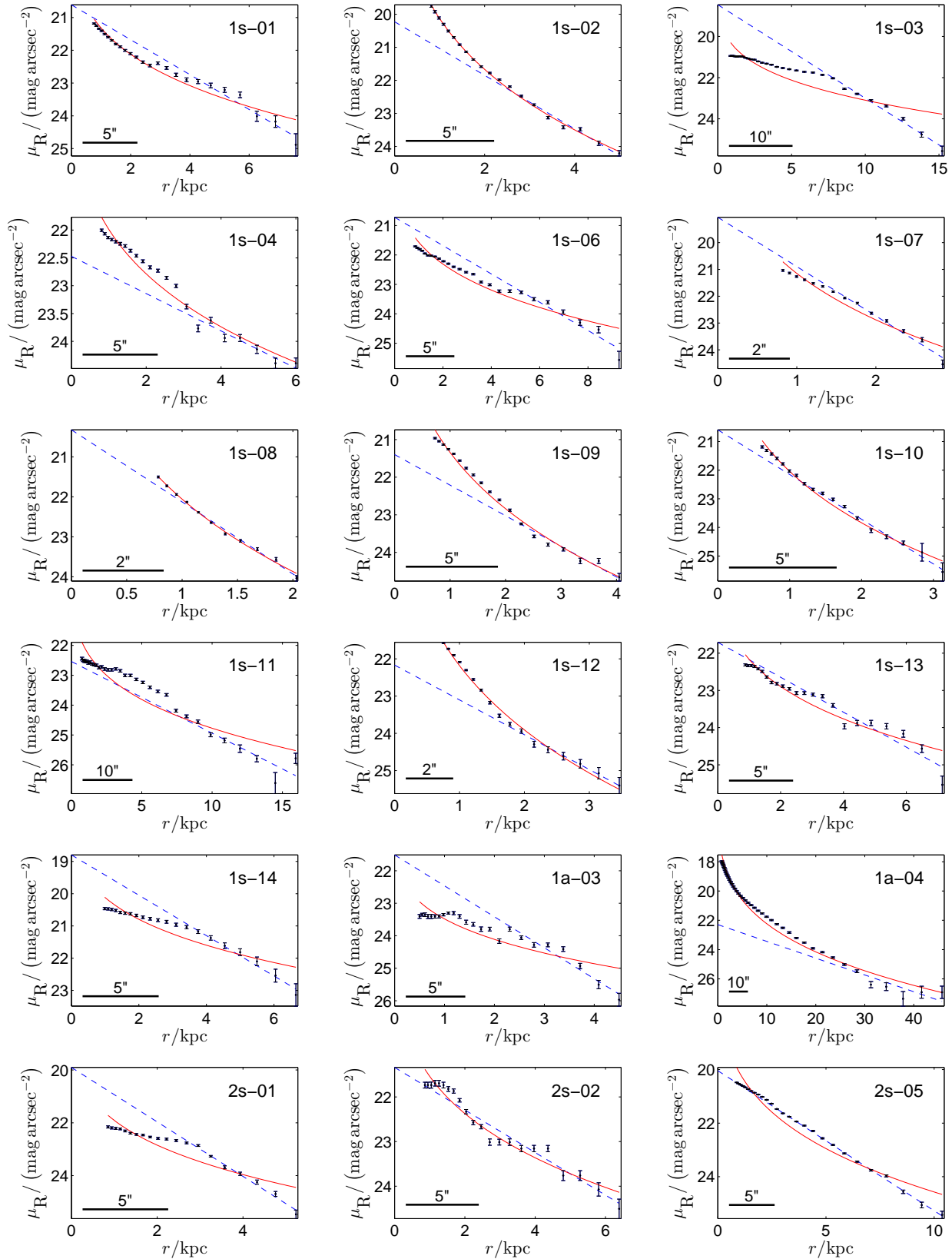
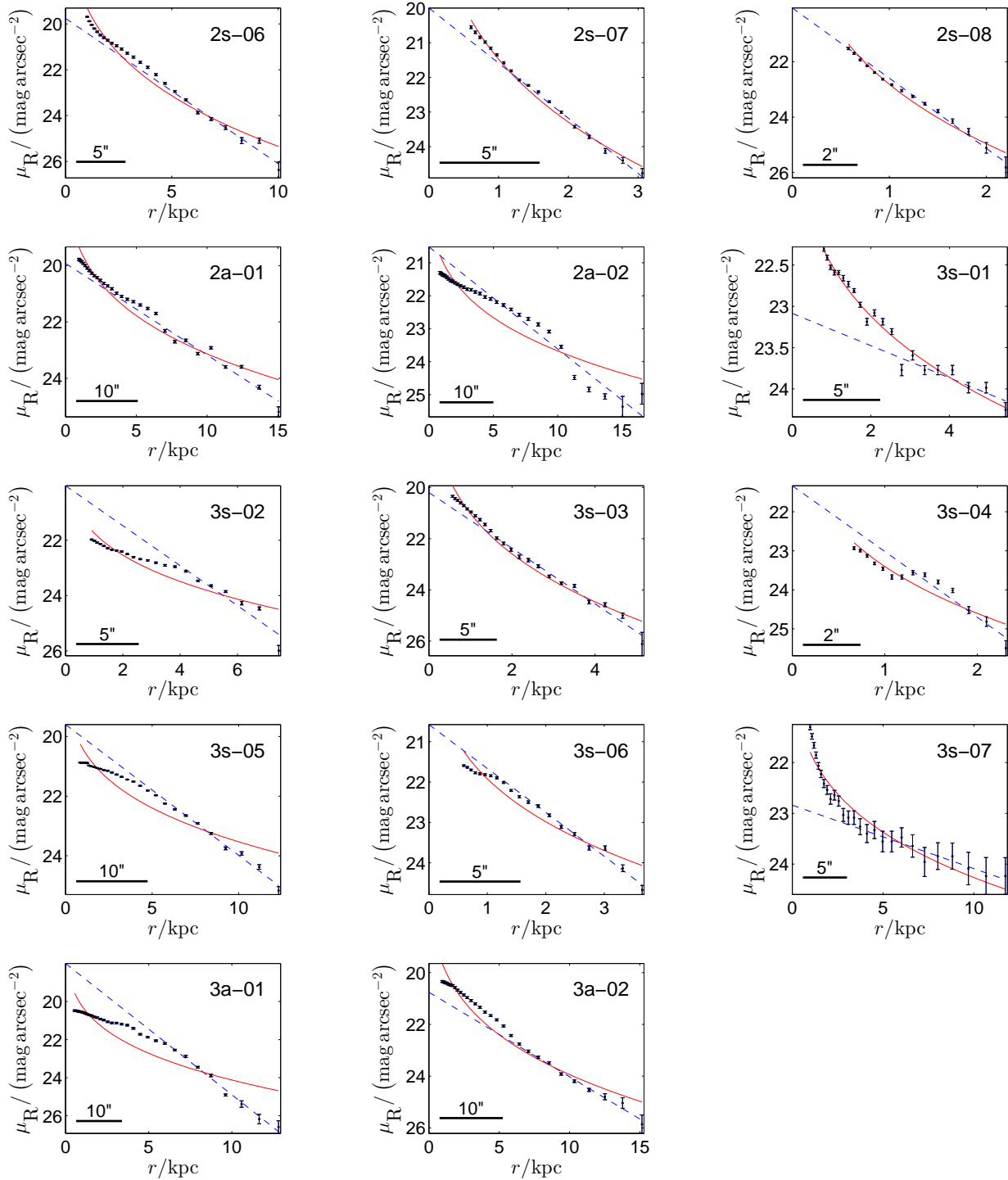


Figure 4. R surface brightness, μ_R , as function of the distance from the galactic centre, r . The black horizontal bars show the angular scale. The blue dashed lines are linear relations, fitted to the points above half of the maximum shown r . The red solid curves show best fits to a de Vaucouleurs formula.

Figure 4 – *continued*

component is not detectable in the nH_α images, even though the total H_α EW, shown in table 8, is considerable. This is a result of noise in the nH_α images, which was reduced in the EW measurements by averaging over the whole galaxy. This noise is significantly less considerable in the R images, because the spectral width of the R filter is more than an order of magnitude larger than the nH_α EW of the EIGs for which H_α emission is not easily detectable in the nH_α images.

The fact that diffused H_α is the dominant component in most EIGs indicates that a possible active galactic nucleus (AGN) contribution to the H_α flux is insignificant. This is supported by the fact that SDSS did not classify any of the EIGs' measured spectra as containing detectable AGN emission lines. Since the H_α measurements utilize narrow bands they include a contribution of the [NII] lines flanking the H_α line. For the central parts of the 22 EIGs which have SDSS spectra this correction was found to be:

Table 7. ALFALFA HI data: EIG name, velocity width of the HI line profile (W_{50}), total HI line flux (F_{HI}), estimated signal to noise ratio of the detection (SNR), HI mass content (M_{HI}) and the category of the HI detection (Code).

EIG	W_{50} [km s ⁻¹]	F_{HI} [Jy km s ⁻¹]	SNR	$\log \frac{M_{HI}}{M_{\odot}}$	Code
1s-01	176 ± 6	1.64 ± 0.07	12.6	9.35 ± 0.02	1
1s-02	65 ± 18	0.66 ± 0.05	8.0	9.01 ± 0.03	1
1s-03	275 ± 3	2.47 ± 0.09	15.3	9.66 ± 0.02	1
1s-04	160 ± 3	1.30 ± 0.07	10.8	9.32 ± 0.02	1
1s-05	32 ± 11	0.46 ± 0.05	8.1	8.84 ± 0.05	1
1s-06	201 ± 8	1.36 ± 0.08	9.3	9.34 ± 0.03	1
1s-07	156 ± 7	0.59 ± 0.05	6.4	8.95 ± 0.04	2
1s-09	91 ± 5	0.96 ± 0.06	9.6	9.03 ± 0.03	1
1s-10	109 ± 9	0.63 ± 0.06	6.1	8.76 ± 0.04	1
1s-14	64 ± 20	0.55 ± 0.06	6.4	9.05 ± 0.05	2
1a-01	196 ± 24	1.78 ± 0.07	13.4	9.49 ± 0.02	1
1a-02	171 ± 36	1.18 ± 0.08	9.8	9.33 ± 0.03	1
1a-03	29 ± 1	0.79 ± 0.03	16.4	8.65 ± 0.02	1
1a-05	254 ± 5	1.47 ± 0.08	9.9	9.37 ± 0.02	1
1a-07	142 ± 26	1.86 ± 0.08	15.7	8.82 ± 0.02	1
2s-02	120 ± 3	2.77 ± 0.08	23.5	9.68 ± 0.01	1
2s-04	153 ± 8	1.10 ± 0.08	9.4	9.30 ± 0.03	1
2s-05	129 ± 11	2.50 ± 0.06	23.1	9.65 ± 0.01	1
2s-06	119 ± 19	0.77 ± 0.07	6.8	9.22 ± 0.04	1
2a-01	154 ± 6	1.65 ± 0.07	13.9	9.49 ± 0.02	1
2a-02	222 ± 17	2.81 ± 0.08	19.4	9.70 ± 0.01	1
2a-03	155 ± 4	1.31 ± 0.08	9.9	9.45 ± 0.03	1
2a-04	117 ± 25	1.07 ± 0.06	10.4	8.97 ± 0.02	1
3s-01	66 ± 8	0.83 ± 0.05	12.2	9.11 ± 0.03	1
3s-02	199 ± 66	0.72 ± 0.08	5.1	9.14 ± 0.05	2
3s-03	69 ± 15	2.26 ± 0.09	25.7	9.23 ± 0.02	1
3s-04	125 ± 10	0.97 ± 0.07	7.6	8.97 ± 0.03	1
3s-05	176 ± 9	1.19 ± 0.08	8.7	9.31 ± 0.03	1
3s-06	113 ± 10	0.65 ± 0.06	6.3	8.69 ± 0.04	1
3s-07	206 ± 7	1.90 ± 0.09	12.2	9.65 ± 0.02	1
3a-01	196 ± 19	3.68 ± 0.08	26.5	9.442 ± 0.009	1
3a-02	296 ± 3	3.02 ± 0.09	18.1	9.79 ± 0.01	1

$\log (F_{H\alpha}/F_{H\alpha+[NII]}) = -0.07 \pm 0.05$ (with 0.95 confidence level). The correction factor for a whole galaxy is expected to be significantly lower than this value, since central parts of galaxies typically have high metal abundance and high [NII] to $H\alpha$ flux ratio compared to those measured for whole galaxies. This difference in the correction factor is expected to be more significant for EIGs in which the diffused $H\alpha$ is the dominant component. In light of this we chose not to correct for these effects.

4.3 Model fitting

The SFH, dust attenuation and stellar mass of the EIGs were estimated by fitting a five-parameter model to their UV-to-near-IR spectral energy distributions (SEDs). The model assumes that the SFH can be described by a first population of stars with an exponentially decreasing or increasing star formation rate (SFR), and a possible addition to recent star formation (a second population). The second population is modelled as an instantaneous star formation that occurred 1 Myr ago and is meant to compensate for a possible recent

deviation from an exponential SFH, which may have a significant effect on the emission from the galaxy (especially in the UV and $H\alpha$). The model can also describe a scenario of a constant star formation or a sudden star formation (first population) with or without a recent star formation burst (second population). This model is obviously a simplification of the actual SFH and is limited in the diversity of possible scenarios. However, not much more can be done given the available SED measured points.

The five free parameters of the model are:

M_1 - The mass of the first population of stars, created along the history of the galaxy (integral over time of the SFR of the first population).

Age_1 - The look-back time of the beginning of star formation of the first population.

τ - The e-folding time of the exponentially decreasing (positive τ) or increasing (negative τ) SFH of the first population. $\tau \ll Age_1$ indicates a sudden star formation, while $\tau \gg Age_1$ indicates an almost constant star formation.

Table 8. Star formation measurements: EIG name, equivalent width (EW), H α flux ($F_{\text{H}\alpha}$), WISE magnitudes (m_{W3} and m_{W4}), fraction of the total H α flux extinguished within the EIG ($\text{frac}_{\text{H}\alpha,\text{ext}}$) and the SFR.

EIG	EW [Å]	$F_{\text{H}\alpha}$ [ergs cm $^{-2}$ s $^{-1}$]	m_{W3}^a	m_{W4}^a	$\text{frac}_{\text{H}\alpha,\text{ext}}^a$	SFR [M_{\odot} yr $^{-1}$]
1s-01	50 ± 5	(4.0 ± 0.9) 10 $^{-14}$	>11.9	>8.4	<0.12	0.16 ± 0.04
1s-02	40 ± 2	(6.3 ± 1.3) 10 $^{-14}$	9.9 ± 0.3	7.4 ± 0.4	0.3 ± 0.1	0.45 ± 0.07
1s-03	27 ± 3	(4.4 ± 1.0) 10 $^{-14}$	10.25 ± 0.05	7.9 ± 0.2	0.34 ± 0.05	0.38 ± 0.06
1s-04	26 ± 4	(1.0 ± 0.3) 10 $^{-14}$	>12.0	>9.0	<0.43	0.05 ± 0.01
1s-06	39 ± 5	(3.0 ± 0.7) 10 $^{-14}$	>11.6	>8.1	<0.23	0.14 ± 0.04
1s-07	40 ± 12	(1.7 ± 0.6) 10 $^{-14}$	11.4 ± 0.4	>8.4	0.3 ± 0.1	0.11 ± 0.03
1s-08	137 ± 16	(3.9 ± 0.9) 10 $^{-14}$	11.4 ± 0.4	>7.9	0.16 ± 0.07	0.20 ± 0.04
1s-09	43 ± 6	(2.4 ± 0.6) 10 $^{-14}$	>12.4	>9.0	<0.13	0.08 ± 0.02
1s-10	75 ± 3	(1.9 ± 0.1) 10 $^{-14}$	12.3 ± 0.5	8.6 ± 0.5	0.16 ± 0.09	0.063 ± 0.007
1s-11	28 ± 4	(2.0 ± 0.7) 10 $^{-14}$	>12.6	>9.0	<0.13	0.08 ± 0.03
1s-12	170 ± 24	(3.2 ± 0.2) 10 $^{-14}$	>12.1	>9.1	<0.13	0.13 ± 0.01
1s-13	48 ± 9	(1.3 ± 0.2) 10 $^{-14}$	>12.3	>9.0	<0.27	0.07 ± 0.01
1s-14	34 ± 7	(8.2 ± 2.5) 10 $^{-14}$	9.3 ± 0.3	7.3 ± 0.4	0.4 ± 0.1	0.9 ± 0.2
1a-03	39 ± 10	(1.6 ± 0.5) 10 $^{-14}$	>12.0	>8.9	<0.24	0.03 ± 0.01
1a-04	4.6 ± 0.4	(13.8 ± 1.7) 10 $^{-14}$	9.21 ± 0.09	7.5 ± 0.4	0.27 ± 0.04	0.95 ± 0.09
2s-01	51 ± 4	(1.5 ± 0.1) 10 $^{-14}$	>12.2	>8.8	<0.26	0.070 ± 0.008
2s-02	23 ± 5	(1.4 ± 0.4) 10 $^{-14}$	>11.7	>8.2	<0.40	0.07 ± 0.02
2s-05	51 ± 3	(12.2 ± 2.6) 10 $^{-14}$	10.5 ± 0.3	8.7 ± 0.4	0.11 ± 0.03	0.7 ± 0.1
2s-06	58 ± 3	(7.1 ± 0.5) 10 $^{-14}$	9.5 ± 0.3	6.3 ± 0.4	0.4 ± 0.2	0.8 ± 0.1
2s-07	58 ± 4	(3.1 ± 0.2) 10 $^{-14}$	9.3 ± 0.3	5.9 ± 0.4	0.7 ± 0.4	0.23 ± 0.07
2s-08	460 ± 39	(11.4 ± 2.5) 10 $^{-14}$	11.3 ± 0.4	7.6 ± 0.4	0.07 ± 0.04	0.30 ± 0.06
2a-01	13.1 ± 0.7	(4.2 ± 0.5) 10 $^{-14}$	8.44 ± 0.01	6.52 ± 0.06	0.72 ± 0.07	0.94 ± 0.06
2a-02	19 ± 1	(1.7 ± 0.3) 10 $^{-14}$	11.3 ± 0.4	>7.9	0.3 ± 0.1	0.16 ± 0.02
3s-01	37 ± 6	(1.4 ± 0.4) 10 $^{-14}$	12.6 ± 0.6	9.2 ± 0.6	0.2 ± 0.1	0.08 ± 0.02
3s-02	28 ± 4	(1.3 ± 0.3) 10 $^{-14}$	>12.2	>8.8	<0.28	0.07 ± 0.02
3s-03	71 ± 3	(13.4 ± 1.5) 10 $^{-14}$	11.1 ± 0.4	8.1 ± 0.4	0.08 ± 0.03	0.33 ± 0.04
3s-04	73 ± 14	(0.5 ± 0.2) 10 $^{-14}$	>12.6	>9.1	<0.46	0.016 ± 0.005
3s-05	35 ± 3	(4.4 ± 0.9) 10 $^{-14}$	11.2 ± 0.4	>8.6	0.18 ± 0.07	0.27 ± 0.05
3s-06	26 ± 5	(0.9 ± 0.2) 10 $^{-14}$	>12.7	>9.1	<0.27	0.021 ± 0.004
3s-07	35 ± 7	(1.6 ± 0.5) 10 $^{-14}$	>12.3	>9.3	<0.20	0.12 ± 0.04
3a-01	48 ± 2	(13.9 ± 0.9) 10 $^{-14}$	12.2 ± 0.5	>8.9	0.03 ± 0.01	0.33 ± 0.02
3a-02	33 ± 2	(6.8 ± 1.0) 10 $^{-14}$	10.06 ± 0.03	8.1 ± 0.2	0.25 ± 0.03	0.67 ± 0.07

^a ‘<’ and ‘>’ indicate 0.95 confidence level upper and lower limits (respectively).**Table 9.** Fraction of the EIG’s total H α flux within regions of interest shown in the last column of figures 1, 2 and 3

EIG	a	b	c	d	e
1s-01	0.13 ± 0.04	0.12 ± 0.04	-	-	-
1s-03	0.11 ± 0.04	0.13 ± 0.05	0.13 ± 0.04	-	-
1s-06	0.13 ± 0.04	-	-	-	-
1s-14	0.5 ± 0.2	0.4 ± 0.1	0.07 ± 0.03	-	-
1a-04	0.6 ± 0.1	-	-	-	-
2s-01	0.27 ± 0.03	0.28 ± 0.05	-	-	-
2s-05	0.07 ± 0.02	0.06 ± 0.02	0.04 ± 0.01	0.13 ± 0.04	0.10 ± 0.03
2s-07	0.90 ± 0.09	-	-	-	-
2a-01	0.22 ± 0.04	0.6 ± 0.1	-	-	-
2a-02	0.33 ± 0.07	0.15 ± 0.04	-	-	-
3s-02	0.21 ± 0.07	0.11 ± 0.04	-	-	-
3s-03	0.32 ± 0.05	0.29 ± 0.05	-	-	-
3s-05	0.3 ± 0.1	0.20 ± 0.06	-	-	-
3s-07	0.20 ± 0.08	0.3 ± 0.1	-	-	-
3a-01	0.18 ± 0.02	0.16 ± 0.02	0.19 ± 0.06	-	-

Table 10. EW [\AA] within regions of interest shown in the last column of figures 1, 2 and 3

EIG	a	b	c	d	e
1s-01	71 ± 6	45 ± 3	-	-	-
1s-03	31 ± 2	23 ± 1	30 ± 3	-	-
1s-06	45 ± 4	-	-	-	-
1s-14	30 ± 5	49 ± 5	26 ± 3	-	-
1a-04	3.2 ± 0.3	-	-	-	-
2s-01	67 ± 7	112 ± 17	-	-	-
2s-05	100 ± 6	70 ± 4	48 ± 2	61 ± 2	104 ± 4
2s-07	73 ± 3	-	-	-	-
2a-01	17 ± 1	11.8 ± 0.5	-	-	-
2a-02	18 ± 1	21 ± 2	-	-	-
3s-02	119 ± 28	22 ± 5	-	-	-
3s-03	75 ± 2	172 ± 6	-	-	-
3s-05	39 ± 2	38 ± 3	-	-	-
3s-07	56 ± 15	26 ± 3	-	-	-
3a-01	26 ± 1	37 ± 1	140 ± 5	-	-

$E(B - V)$ - The $(B - V)$ colour excess that results from dust within the galaxy.

M_2 - The mass of the second population of stars that was created.

The model fitting procedure used Bayesian statistical inference with uniform prior probability distributions of $\log(M_1)$, $\log(Age_1)$, τ^{-1} , $E(B - V)$ and $\log(M_2)$. The parameters were restricted to the following ranges: $10^7 M_\odot < M_1 < 1.6 \cdot 10^{15} M_\odot$, $10^8 \text{ yr} < Age_1 < \text{age of the Universe at the redshift of the galaxy}$, $0 < E(B - V) < 2$, $2.7 M_\odot < M_2 < 10^7 M_\odot$. The metallicities of the first and second populations were set to $0.4 Z_\odot$ and $1 Z_\odot$ respectively.

The model fitting was computed using the GalMC software (Acquaviva et al. 2011a,b)¹⁰. GalMC is a Markov Chain Monte Carlo (MCMC) algorithm designed to fit the SEDs of galaxies to infer physical properties such as age, stellar mass, dust reddening, metallicity, redshift, and star formation rate. The Markov chains produced by GalMC were analysed using the GetDist software, a part of the CosmoMC software (Lewis & Bridle 2002)¹¹.

The stellar emission was calculated using the Charlot & Bruzual 2007 stellar population synthesis model (Charlot & Bruzual, private communication, CB07¹²) assuming a Salpeter initial mass function. Nebular emission was calculated following Schaerer & Vacca (1998) and Schaerer & de Barros (2009), as described in section 2.2.4 of Acquaviva et al. (2011b). Dust extinction within the EIG was calculated from the $E(B - V)$ parameter using the Calzetti et al. (1994) law with $R_v = 4.05$ (Calzetti et al. 2000). The emission of the EIGs were also corrected for absorption by neutral hydrogen in the intergalactic medium (IGM) using Madau (1995).

The input to the model-fitting software included the

EIG's redshift and the data from measured bands with wavelengths shorter than $3 \mu\text{m}$ (the CB07 model does not estimate correctly the emission beyond the first PAH feature at $\sim 3 \mu\text{m}$). Each band measurement was corrected for Galactic extinction and then converted to flux, which was used as input to the GalMC software. The calibrated Bessell U, B, V, R and I magnitudes, measured at the Wise Observatory, were translated to AB magnitudes (and then to flux) using the relations listed in Table 1 of Blanton & Roweis (2007). The 2MASS magnitudes were converted to fluxes using the zero magnitude isophotal monochromatic intensities listed in Table 2 of Cohen et al. (2003). Foreground Galactic extinction was corrected as described in section 3.5.

For each EIG four MCMC runs were made, each with a different set of free parameters as a starting point. Best-fitting parameters and covariance matrices of these four runs were then used as inputs for continued runs. Each run included 50000 sampled parameter sets. Only one of each EIG's MCMC runs (chains) was used for analysis. This run was chosen based on the speed of convergence of the chain, on its average likelihood, on its multiplicity (number of trial steps before moving to the next location in parameter space), and on how well it covered the parameter space. Chains that probed the parameter space with $Age_1 < 0.2 \text{ Gyr}$ for a large fraction of their length were disfavoured (if another good chain existed it was selected instead of them).

Models were not fitted to EIG 1s-05 and EIG 2s-04, because these do not have the necessary SED data. EIG 1s-05 has only 21 cm data, and EIG 2s-04 has only g , r , i and z measurements (due to a bright foreground star close to it). The model that was fitted to EIG 1s-11 did not reproduce its H_α emission successfully ($EW = 28 \pm 4 \text{ \AA}$). The best-fitting parameters of all MCMC runs of EIG 1s-11 yielded lower EW values.

Marginalized posterior distributions (the predicted probability distribution functions, PDFs) of the free parameters and of the calculated total mass of stars, M_* , consider-

¹⁰ <http://ctp.citytech.cuny.edu/~vacquaviva/web/GalMC.html>

¹¹ <http://cosmologist.info/cosmomc/>

¹² <http://www.bruzual.org/>

ing mass-loss mechanisms, were calculated from the selected chain of each EIG. Figure B1 in Appendix B shows, for each of the modelled EIGs, the marginalized posterior distributions of Age_1 , τ^{-1} , $E(B - V)$, M_2 and M_* . Table 11 lists the M_* values predicted by the model.

Two-dimensional marginalized PDFs of pairs of the model parameters were also analysed. It was found that in most cases there is some dependence between pairs of the free parameters. The M_1 and Age_1 parameters were found to be highly correlated. The (Age_1, M_1) two-dimensional marginalized PDFs do not seem to depend on whether they are part of the EIG-1, EIG-2 or EIG-3 subsample, i.e. the (Age_1, M_1) space is filled similarly by the three subsamples.

4.4 Dynamic mass

We estimated dynamic mass lower limits for the EIGs using the ALFALFA measured HI rotation, the elliptical isophotes fitted to the combined R images (described in section 3.4) and the surface brightness measurements, μ_R . The calculations were based on the methods described by Courteau et al. (2014). First, we estimated the inclination of the galaxies using eq. 6 of Courteau et al. (2014) for the $\mu_R = 24$ mag arcsec $^{-2}$ elliptical isophote:

$$i \cong \cos^{-1} \sqrt{\frac{(b_{24}/a_{24})^2 - q_0^2}{1 - q_0^2}} \quad (6)$$

where:

- i is the estimated inclination of the galaxy;
- a_{24} , b_{24} are the semi-major axis and semi-minor axis (respectively) at $\mu_R = 24$ mag arcsec $^{-2}$;
- q_0 is the axial ratio of a galaxy viewed edge on.

The inclination of EIGs classified as early-types was not measured, because their q_0 is unknown. For a sample of 13482 spiral galaxies Lambas et al. (1992) found $q_0 \cong 0.2$ by applying statistical techniques to explore triaxial models. Hall et al. (2012) found $q_0 \cong 0.13$ for spirals using SDSS data on a sample of 871 edge-on galaxies. Here we adopted $q_0 = 0.17 \pm 0.05$ for the galaxies classified as late-types or ‘unknown’ (see table 4).

we measured a_{24} using the linear fit of figure 4. The semi-minor to semi-major axes ratio, b_{24}/a_{24} , was calculated by linear interpolation of its values for the EIG’s ellipse isophotes just below and just above a_{24} . The speed of rotation of the HI gas, v_{rot} , was calculated using the HI velocity width, W_{50} , listed in Table 7 and the inclination, i , using:

$$v_{rot} = \frac{W_{50}}{2 \cdot \sin i} \quad (7)$$

The dynamic mass lower limit, $M_{dyn,24}$, was then calculated using:

$$M_{dyn,24} = \frac{v_{rot}^2 \cdot a_{24}}{G} \quad (8)$$

$M_{dyn,24}$ is a lower limit to the galactic total mass, since the extent of the neutral gas in spiral galaxies can often exceed twice that of the stars (Courteau et al. 2014), and

the dark matter (DM) halo may extend even further. An additional source of uncertainty in $M_{dyn,24}$ comes from the assumption behind (7) that all of the HI velocity width, W_{50} , is due to the rotational velocity, v_{rot} . This may somewhat increase the $M_{dyn,24}$ estimate, but probably by much less than it is decreased due to the underestimation of the dark mass diameter. Table 12 lists $M_{dyn,24}$ of EIGs along with the values used for its calculation. It also lists the ratio of the measured dynamic mass to stellar plus HI mass, $M_{dyn,24}/(M_* + M_{HI})$.

5 ANALYSIS

5.1 Colours of the EIGs

Colour-mass and colour-colour diagrams of large scale surveys show that galaxies tend to populate two main regions, the ‘blue cloud’ of star-forming galaxies and the ‘red sequence’ of quiescent galaxies, with a small fraction of galaxies in a ‘green valley’ range in between (Strateva et al. 2001; Baldry et al. 2006; Schawinski et al. 2014). Star-forming main sequence galaxies populate the blue cloud, whether their star formation started recently or a long time ago. When star formation is quenched, galaxies leave the main sequence and their changing colours can be interpreted as a reflection of the quenching process (Schawinski et al. 2014).

Figure 5 shows a $(u - r)$ to M_* colour-mass diagram of the EIGs, with the approximate edges of the ‘green valley’ marked in green bold lines. The $(u - r)$ colour was corrected both for Galactic extinction (as described in section 3.5), and for dust within the EIG using the Calzetti et al. (2000) extinction law (with $R'_V = 4.05$).

It is evident from Figure 5 that most EIGs are ‘blue cloud’ galaxies. There are no EIGs in the ‘red sequence’ and only one that is certainly within the ‘green valley’ (EIG 1a-04). Based on comparison between the measurements and the ‘green valley’ limit shown in Figure 5, we can conclude with 0.95 confidence that the probability for an EIG to be in the ‘blue cloud’ is >0.76 . The probability for an EIG to be in the ‘red sequence’ is <0.12 .

A linear relation was fitted to the measured EIG points of Figure 5 (the thin blue line in the figure): $(u - r)_{dust\ corrected} = 0.52 \cdot \log(M_*/M_\odot) - 3.61$. The expected standard deviation in $(u - r)$ around this fit is 0.23 mag (marked in the figure by dashed blue lines). The 0.52 slope of this fit is significantly larger than the slope of the ‘green valley’ limits, 0.25 (Schawinski et al. 2014). It can be concluded from this that the EIGs will be closer to the ‘red sequence’, the higher their stellar mass, M_* , is. EIGs with stellar mass smaller than $10^{(10.6 \pm 0.9)} M_\odot$ are typically ‘blue cloud’ galaxies.

A similar colour-mass relation probably holds also for less isolated galaxies, as indicated by the results of Fernández Lorenzo et al. (2012) who studied the AMIGA sample. They have measured colour-luminosity correlation in different morphological subtypes, and found that the more massive spirals show redder colours, and that there is little evidence for ‘green valley’ galaxies in the AMIGA sample.

Figure 6 shows an $(NUV - u)$ vs. $(u - r)$ colour-colour diagram of the EIGs, with the approximate limit between

Table 11. Modelled Stellar Mass

EIG	$\log \frac{M_*}{M_\odot}$	EIG	$\log \frac{M_*}{M_\odot}$	EIG	$\log \frac{M_*}{M_\odot}$	EIG	$\log \frac{M_*}{M_\odot}$
1s-01	8.9 ± 0.1	1s-12	8.0 ± 0.1	2s-05	9.7 ± 0.2	3s-03	8.7 ± 0.1
1s-02	9.3 ± 0.1	1s-13	8.3 ± 0.1	2s-06	9.3 ± 0.3	3s-04	7.4 ± 0.1
1s-03	9.5 ± 0.2	1s-14	9.7 ± 0.2	2s-07	8.52 ± 0.05	3s-05	9.3 ± 0.2
1s-04	8.6 ± 0.1	1a-01	9.6 ± 0.2	2s-08	7.3 ± 0.1	3s-06	8.20 ± 0.08
1s-06	9.0 ± 0.1	1a-02	9.1 ± 0.2	2a-01	10.5 ± 0.2	3s-07	8.9 ± 0.2
1s-07	9.0 ± 0.2	1a-03	8.3 ± 0.1	2a-02	9.7 ± 0.2	3a-01	9.3 ± 0.1
1s-08	8.5 ± 0.1	1a-04	11.40 ± 0.07	2a-03	9.7 ± 0.2	3a-02	10.1 ± 0.2
1s-09	8.41 ± 0.07	1a-07	8.1 ± 0.1	2a-04	8.3 ± 0.2		
1s-10	8.05 ± 0.08	2s-01	8.6 ± 0.2	3s-01	8.8 ± 0.2		
1s-11	9.1 ± 0.2	2s-02	9.0 ± 0.2	3s-02	8.67 ± 0.06		

Table 12. Dynamic mass

EIG	a_{24} [kpc]	b_{24}/a_{24}	i [deg]	v_{rot} [km s ⁻¹]	$\log \frac{M_{dyn,24}}{M_\odot}$	$\frac{M_{dyn,24}}{M_* + M_{HI}}$
1s-01	6.4 ± 0.4	0.46 ± 0.02	64 ± 2	98 ± 4	10.15 ± 0.04	3.8 ± 0.4
1s-03	12.2 ± 0.4	0.231 ± 0.009	81 ± 3	139 ± 2	10.74 ± 0.02	6.0 ± 0.5
1s-04	4.6 ± 0.4	0.57 ± 0.03	56 ± 2	96 ± 3	9.99 ± 0.04	3.1 ± 0.3
1s-06	6.8 ± 0.5	0.48 ± 0.02	63 ± 2	113 ± 5	10.31 ± 0.05	5.2 ± 0.7
1s-07	2.69 ± 0.09	0.92 ± 0.08	24 ± 11	191 ± 79	10.4 ± 0.4	10 ± 8
1s-10	2.18 ± 0.08	0.95 ± 0.04	19 ± 7	166 ± 57	10.1 ± 0.3	16 ± 11
1s-14	8.3 ± 0.3	0.81 ± 0.04	37 ± 4	54 ± 17	9.7 ± 0.3	0.9 ± 0.6
1a-03 ^a	2.6 ± 0.2	0.90 ± 0.05	27 ± 7	32 ± 7	8.8 ± 0.2	0.8 ± 0.4
2s-02	5.6 ± 0.4	0.85 ± 0.07	33 ± 8	111 ± 22	10.2 ± 0.2	2.2 ± 0.9
2s-05	7.6 ± 0.2	0.82 ± 0.02	35 ± 2	112 ± 10	10.35 ± 0.08	2.1 ± 0.5
2s-06	6.7 ± 0.4	0.58 ± 0.02	56 ± 1	72 ± 11	9.9 ± 0.1	1.8 ± 0.7
2a-01	13 ± 1	0.30 ± 0.02	75 ± 2	80 ± 3	10.27 ± 0.05	0.6 ± 0.2
2a-02	11 ± 2	0.29 ± 0.01	76 ± 2	114 ± 9	10.53 ± 0.09	3.0 ± 0.7
3s-02	5.5 ± 0.5	0.56 ± 0.02	57 ± 2	119 ± 39	10.3 ± 0.3	8 ± 5
3s-03	3.5 ± 0.2	0.78 ± 0.02	39 ± 2	55 ± 12	9.4 ± 0.2	0.9 ± 0.4
3s-04	1.6 ± 0.1	0.49 ± 0.02	62 ± 2	71 ± 6	9.27 ± 0.08	1.5 ± 0.3
3s-05	10.0 ± 0.3	0.24 ± 0.01	80 ± 3	89 ± 5	10.27 ± 0.05	4.1 ± 0.6
3s-06	3.1 ± 0.1	0.43 ± 0.02	67 ± 2	62 ± 5	9.44 ± 0.08	3.4 ± 0.7
3s-07	9 ± 1	0.24 ± 0.02	80 ± 3	105 ± 4	10.37 ± 0.05	3.5 ± 0.5
3a-01	8.7 ± 0.3	0.217 ± 0.006	82 ± 4	99 ± 10	10.30 ± 0.09	3.6 ± 0.7
3a-02	9.9 ± 0.4	0.367 ± 0.009	71 ± 2	157 ± 2	10.75 ± 0.02	2.9 ± 0.4

^a Due to stars/galaxies projected by chance on EIG 1a-03 and interfering with the measurement b_{24}/a_{24} was measured on the third largest ellipse isophote ($\mu_R = 24.93 \pm 0.08$ mag arcsec⁻²).

the ‘blue cloud’ and the ‘green valley’ marked with a green line (the ‘blue cloud’ is to the left of the line, and the ‘green valley’ is to the right). These colours were corrected for Galactic extinction and dust within the EIG, as in Figure 5. Other than distinguishing between blue and red galaxies, this diagram is useful for diagnosing how rapidly star formation quenches in ‘green valley’ galaxies. The faster the star formation quenching is, the higher the $(NUV - u)$ colour of galaxies would be as their $(u - r)$ is gradually increased (Schawinski et al. 2014, Fig. 7).

The ‘green valley’ galaxy, EIG 1a-04, is significantly redder in both colours, $(u - r) = 2.32 \pm 0.08$ and $(NUV - u) = 3.5 \pm 0.3$, compared to the other EIGs as Figure 6 shows. A comparison to the simulated SFH scenarios from Fig. 7 of Schawinski et al. (2014) shows that EIG 1a-04 fits a scenario of a galaxy that passed, more than 1 Gyr ago, a rapid star formation quenching (with e-folding time significantly

shorter than 1 Gyr). The model fitted in this work (see Figure B1, page 38, row 8) matches this scenario. Another evidence supporting this scenario is that EIG 1a-04 was not detected by ALFALFA. This indicates that it might have lost most of its HI content which, given its extremely high stellar mass, perhaps was once very high. It should be noted in this context that EIG 1a-04 is possibly not an extremely isolated galaxy (a possible false positive) as discussed in Appendix A. Its H α images show that LEDA 213033, a galaxy separated by $\sim 2'$ from it, may be a neighbour less than 300 km s⁻¹ away.

Other EIGs with less than 0.90 confidence of being in the ‘blue cloud’ are 2s-02, 2s-07, and 1s-11 (calculated from data shown in Figure 5). From Figure 6 it is evident that EIG 1s-11 (as well as EIG 2a-01) deviate towards the red section. EIG 2s-02 is somewhat redder in $(u - r)$ or bluer in $(NUV - u)$ than the bulk. EIG 2s-07 seems to be well

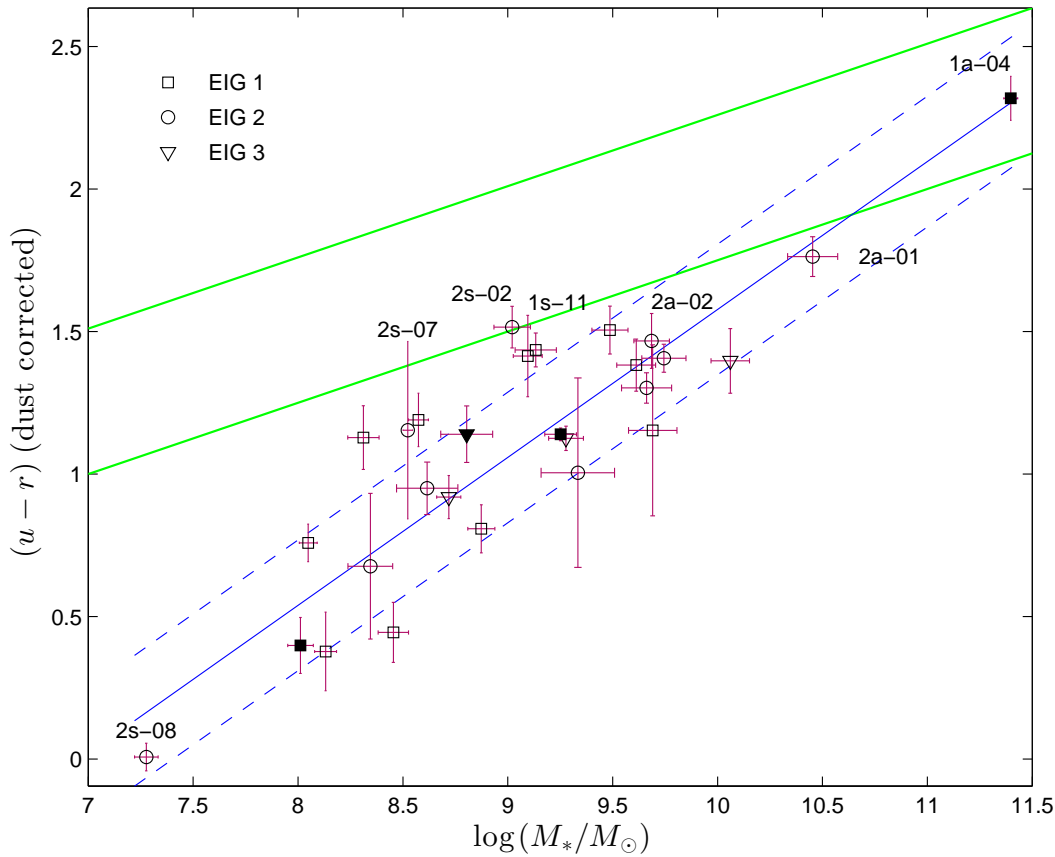


Figure 5. Colour-to-stellar mass diagram. $(u - r)$, corrected for both Galactic extinction and dust extinction within the EIG, as function of stellar mass, M_* . The green thick lines show the limits of the ‘green valley’, based on equations (1) and (2) of Schawinski et al. (2014). The thin blue line shows a linear fit to the EIG data. The dashed blue lines show the $\pm 1\sigma$ deviation from this fit. Filled symbols indicate EIGs classified as early-types.

within the bulk of EIGs in Figure 6, which indicates that it is a regular ‘blue cloud’ galaxy (data of Figure 5 indicates 0.77 probability that it is in the ‘blue cloud’).

5.2 Comparison to the main sequence of star-forming galaxies

Most star-forming galaxies exhibit a tight, nearly linear correlation between galaxy stellar mass and SFR (on a log-log scale; Noeske et al. 2007). This correlation is termed ‘the main sequence of star-forming galaxies’ (or simply ‘the main sequence’). Up to redshifts $z \sim 2$ the correlation changes only in its normalization (Lee et al. 2012; Schawinski et al. 2014). Models of Bouché et al. (2010) and Lilly et al. (2013) suggest that the main sequence is a result of an equilibrium between galaxy inflows and outflows.

For a specific range of redshift, z , and stellar mass, M_* , the main sequence can be expressed as:

$$\log\left(\frac{\text{SFR}}{M_\odot \text{ yr}^{-1}}\right) = \alpha \cdot \log\left(\frac{M_*}{M_\odot}\right) + \beta \quad (9)$$

where:

α , β are the free parameters fitted to the observed data.

The α and β parameters somewhat vary with redshift. Salim et al. (2007) and Huang et al. (2012) indicated that below $\log(M_*) \sim 9.5$ the slope, α , of the main sequence increases. Huang et al. (2012) have studied a sample of local Universe ALFALFA galaxies with SDSS and GALEX photometry and have found the following main sequence relation:

$$\alpha = \begin{cases} 0.851 & \text{for } \log(M_*/M_\odot) \leq 9.5 \\ 0.241 & \text{for } \log(M_*/M_\odot) > 9.5 \end{cases}$$

$$\beta = \begin{cases} -8.207 & \text{for } \log(M_*/M_\odot) \leq 9.5 \\ -2.402 & \text{for } \log(M_*/M_\odot) > 9.5 \end{cases} \quad (10)$$

Figure 7 shows the current SFR (upper plot) and SSFR (lower plot) of the EIGs as function of stellar mass, M_* , compared to the ‘main sequence’ of Huang et al. (2012). It indicates that, in general, EIGs fit the ‘main sequence of star-forming galaxies’. A fraction of $0.88^{+0.08}_{-0.16}$ of the EIGs fit the ‘main sequence’ to within ± 0.5 dex (assuming that whether an EIG deviates by more than ± 0.5 dex or not follows a binomial distribution, and using a Wilson score interval with 0.95 confidence level). On average, the SFR of the EIGs is 0.1 dex lower than the main sequence, with a standard deviation of 0.4 dex. This deviation from the main

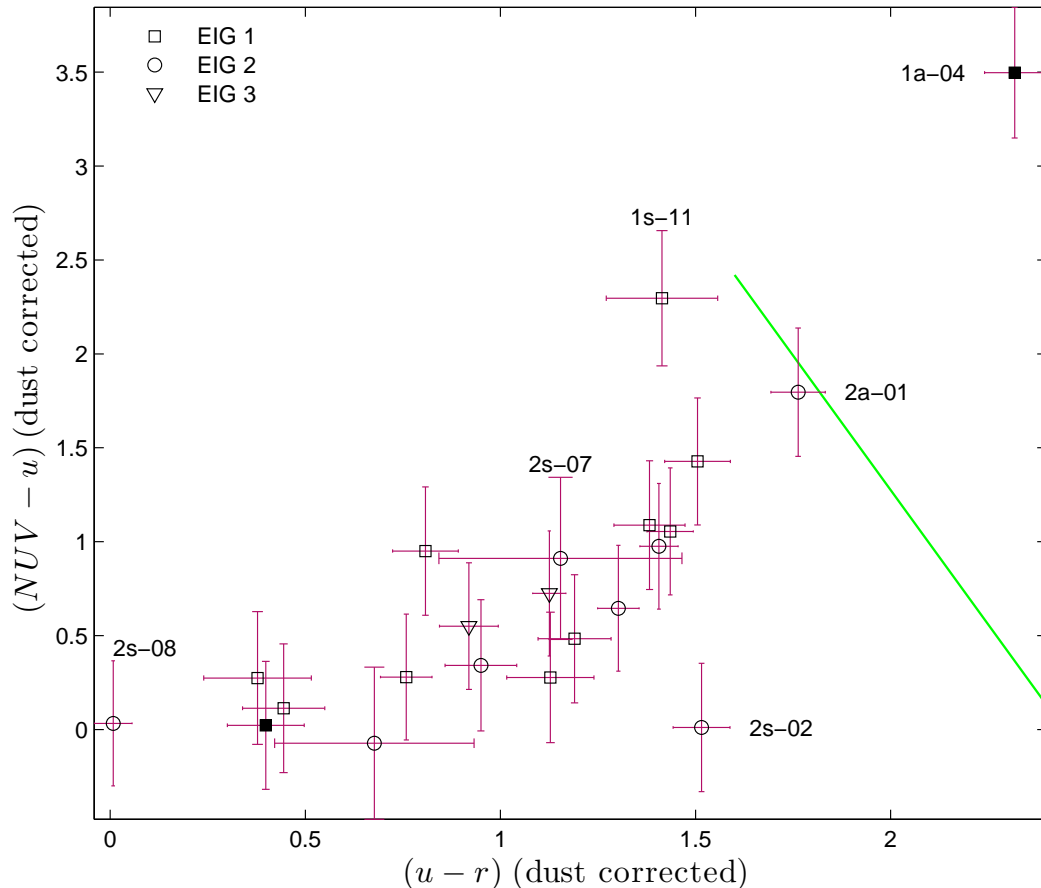


Figure 6. Dust corrected $(NUV - u)$ vs. $(u - r)$ colour-colour diagram of the EIG. The green line shows the approximated limit between the ‘blue cloud’ and the ‘green valley’, based on Fig. 7 of Schawinski et al. (2014) (the ‘blue cloud’ is to the left of the line, and the ‘green valley’ is to the right). Filled symbols indicate EIGs classified as early-types.

sequence is similar for all EIG sub-samples (1, 2 and 3). It may indicate a tendency of the EIGs to have slightly lower SFRs compared to main sequence galaxies. However, it could also result from differences between the SFR and M_* estimation methods used by Huang et al. (2012) and the ones used here. Huang et al. (2012) derived stellar masses and SFRs by SED fitting of the seven GALEX and SDSS bands, while in this work the H_α emission line and 2MASS data were also used when available for the SED fitting. Furthermore, in this work the SED fitting was used only for M_* estimation. The SFR was estimated based on H_α and WISE fluxes.

The EIGs that deviate by more than 0.5 dex in SFR from the main sequence are EIG 1s-11 (-0.7 ± 0.2 dex), EIG 2s-02 (-0.6 ± 0.1 dex), EIG 2s-08 (1.49 ± 0.09 dex) and EIG 2a-02 (-0.73 ± 0.06 dex). EIG 2s-08 is, therefore, the only EIG known to deviate significantly from the main sequence. It has the highest SSFR of all the measured EIGs, $\log(\text{SSFR}/\text{yr}^{-1}) = -7.80 \pm 0.09$, as well as the highest H_α EW ($460 \pm 39 \text{ \AA}$). It also has the lowest stellar mass, $\log(M_*/M_\odot) = 7.28 \pm 0.06$, as well as the lowest model estimated age, $\log(\text{Age}_1/\text{yr}) = 8.4 \pm 0.2$. Based on this we conclude (with 0.95 confidence) that the probability for an EIG to have SFR that deviates significantly from the main sequence is < 0.16 .

For the LOG catalogue of isolated galaxies Karachentsev et al. (2013) measured SSFR values as function of M_* lower than those measured here for the EIGs and lower than the main sequence as measured by Huang et al. (2012). This may be a result of their different method of estimating M_* . Karachentsev et al. (2013) used K_s band measurements assuming a K_s luminosity to stellar mass ratio as that of the Sun, as opposed to fitting a model to measurements in several bands as was done here and by Huang et al. (2012). They also observed that almost all of the LOG galaxies have $\log(\text{SSFR}/\text{yr}^{-1})$ lower than -9.4 (Karachentsev et al. 2013, Fig. 4). As the lower plot of Figure 7 indicates, the $\log(\text{SSFR}/\text{yr}^{-1})$ limit we measured for the EIGs is -8.9 with the exception of EIG 2s-08 that is above this value.

5.3 Mass histograms

The stellar mass, M_* , HI mass, M_{HI} , and dynamic mass, $M_{\text{dyn},24}$, of EIGs were analysed in a fashion similar to that of the analysis of the dark matter (DM) subhalo mass, M_{halo} , of the Millennium II-SW7 simulation (Mill2; Guo et al. 2013) described in section 3.5 of SB16. Figures 8, 9 and 11 show histograms of M_* , M_{HI} and $M_{\text{dyn},24}$ (respectively) for the EIGs of the Spring and Autumn sky regions. Figure 10 shows histograms of $(M_* + M_{\text{HI}})$ of all EIGs for which M_* was es-

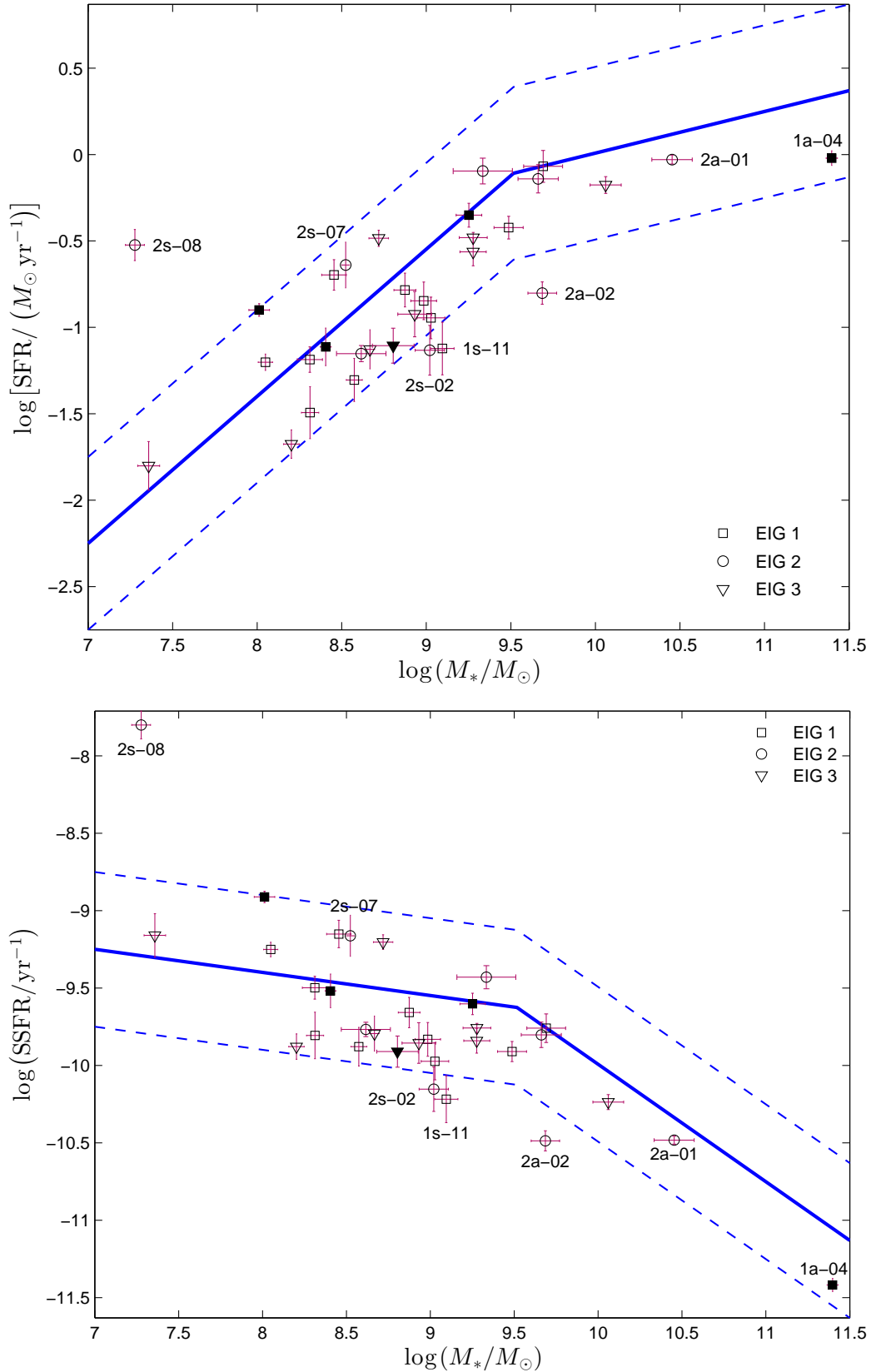


Figure 7. EIGs compared to the main sequence of star-forming galaxies (SFR vs. M_* in the top chart and SSFR vs. M_* in the bottom chart). The solid blue lines are the best fit main sequence found by Huang et al. (2012) and described by (10). The dashed blue lines indicate deviations of ± 0.5 dex from the main sequence (a typical 1σ deviation of main sequence fits). Filled symbols indicate EIGs classified as early-types.

timated. For EIGs not detected by ALFALFA, M_* was used as representing $(M_* + M_{HI})$. Thus the $(M_* + M_{HI})$ statistics presented here, is expected to be slightly biased towards lower masses and a wider distribution. Similarly, Figure 9 includes only EIGs that were detected by ALFALFA, and is, therefore, expected to be slightly biased towards higher masses and a narrower distribution. The right-hand side charts of figures 8, 9, 10 and 11 may be compared to Figure 12, an adaptation of Figure 6 of SB16, which shows the simulation-based estimates of M_{halo} calculated for the combination of subsamples EIG-1 and EIG-2.

As can be seen in these figures, the distributions of both M_* and $(M_* + M_{HI})$ are more scattered than those of M_{halo} . For EIGs in the Spring sky region the standard deviation of $\log [M_{halo}/(h^{-1} M_\odot)]$ is ~ 0.3 , compared to ~ 0.6 for $\log (M_*/M_\odot)$ and ~ 0.7 for $\log [(M_* + M_{HI})/M_\odot]$. For the Autumn EIGs the standard deviation of $\log [M_{halo}/(h^{-1} M_\odot)]$ is ~ 0.4 , compared to ~ 1.1 for $\log (M_*/M_\odot)$ and ~ 0.8 for $\log [(M_* + M_{HI})/M_\odot]$. Such higher scatter of M_* compared to M_{halo} is expected from the stellar mass to halo mass (SMHM) relation derived from simulations (e.g., Fig. 2 of Conroy & Wechsler 2009, Fig. 7 of Behroozi et al. 2013, Fig. 2 of Durkalec et al. 2015, Fig. 5 of Rodríguez-Puebla et al. 2015 and Fig. 1 of Matthee et al. 2017). The vast majority of EIGs have masses $\log (M_*/M_\odot) < 10.5$ and $\log [M_{halo}/(h^{-1} M_\odot)] < 12$ in which the SMHM relation's slope is large, i.e. in which M_* varies faster than M_{halo} . The distribution of the HI mass, M_{HI} , seems to have a width similar to that of M_{halo} (the standard deviation of $\log (M_{HI}/M_\odot)$ is ~ 0.3 for the Spring EIGs and ~ 0.4 for the Autumn EIGs).

The distribution of the simulation predicted M_{halo} (shown in Figure 12) is very different from the distribution of $M_{dyn,24}$ (shown in Figure 11). The average $\log (M_{dyn,24}/M_\odot)$ is ~ 10.2 for the Spring and ~ 9.9 for the Autumn. This is about an order of magnitude lower than the average $\log [M_{halo}/(h^{-1} M_\odot)]$ (11.0 for Spring and 11.3 for Autumn). The standard deviation of $\log (M_{dyn,24}/M_\odot)$ is ~ 0.3 for the Spring EIGs and ~ 0.9 for the Autumn EIGs (compared to ~ 0.3 for the Spring and ~ 0.4 for the Autumn $\log [M_{halo}/(h^{-1} M_\odot)]$). This difference between the simulated distribution of M_{halo} and the measured distribution of $M_{dyn,24}$ may be the result of a large discrepancy between $M_{dyn,24}$ and the actual dynamic mass (had it been measured using HI rotation curves), a large discrepancy of the simulation results from reality, or both.

The average $\log (M_*/M_\odot)$ for EIG-1 and EIG-2 is ~ 8.8 (Spring) and ~ 9.4 (Autumn). From a comparison to the average $\log [M_{halo}/(h^{-1} M_\odot)]$ (11.0 for Spring, and 11.3 for Autumn) we conclude that the stellar masses, M_* , of EIGs are ~ 2.4 dex (Spring) and ~ 2.0 dex (Autumn) lower on average than the EIGs' DM masses. This, compared to a ~ 0.7 dex difference between the baryonic to DM average densities in the Universe (according to WMAP7). If the dark-to-baryonic matter ratio of isolated galaxies is similar to the Universal average, then the geometric average of the fraction of baryonic mass turned into stars is ~ 0.02 (Spring) and ~ 0.05 (Autumn).

It is interesting to compare the stellar and HI content of galaxies from subsample EIG-1 with those of subsample EIG-2. As described in section 1, the EIG-1 subsample

contains galaxies that passed the isolation criterion using both NED and ALFALFA data. The EIG-2 subsample contains galaxies that passed the criterion using NED data, but did not pass it using ALFALFA data (have neighbours closer than $3 h^{-1}$ Mpc with sufficient HI content to be detected by ALFALFA). Therefore, the distance to the closest ALFALFA neighbour for EIG-1 galaxies is $> 3 h^{-1}$ Mpc by definition. For EIG-2 galaxies this distance is in the range $0.66\text{--}2.74 h^{-1}$ Mpc ($0.9\text{--}3.9$ Mpc; see Table 8 of Spector & Brosch 2016).

Figure 13 shows histograms of M_* (left charts), and M_{HI} (right charts) comparing subsample EIG-1s with EIG-2s (upper charts) and subsample EIG-1a with EIG-2a (lower charts). As can be seen, the M_* distribution of EIG-1s is similar to that of EIG-2s, and the distribution of EIG-1a is similar to that of EIG-2a. The average $\log (M_*/M_\odot)$ of the measured EIG-1s galaxies is 8.8 ± 0.1 with a standard deviation of 0.5. This, compared to an average of 8.7 ± 0.3 with standard deviation 0.8 for the measured EIG-2s galaxies. The average $\log (M_*/M_\odot)$ of the measured EIG-1a galaxies is 9.3 ± 0.6 with a standard deviation of 1.3. This, compared to an average of 9.6 ± 0.4 with standard deviation 0.9 for the measured EIG-2a galaxies. These differences are not statistically significant.

In contrast to this, the M_{HI} distributions differ significantly between the EIG-1 and the EIG-2 subsamples. The average $\log (M_{HI}/M_\odot)$ of the EIG-1s galaxies detected by ALFALFA is 9.13 ± 0.09 (with standard deviation 0.3). This, compared to an average of 9.5 ± 0.1 (with standard deviation 0.2) for the ALFALFA-detected EIG-2s galaxies; a 2.3σ difference.

The difference in the average $\log (M_{HI}/M_\odot)$ between the Autumn subsamples is the same as for the Spring subsamples (~ 0.3), but with lower statistical significance (1.2σ) due to the smaller numbers of measured galaxies. The average $\log (M_{HI}/M_\odot)$ of the EIG-1a galaxies detected by ALFALFA is 9.1 ± 0.2 (with standard deviation 0.4). This, compared to an average of 9.4 ± 0.2 (with standard deviation 0.3) for the ALFALFA-detected EIG-2a galaxies.

Combining the differences measured for the Spring and Autumn, gives an expected difference between $\log (M_{HI}/M_\odot)$ of EIG-2 and EIG-1 of 0.3 ± 0.1 dex. Therefore, from the data of the ALFALFA-detected galaxies we conclude with 2.5σ significance that EIG-2 galaxies have higher M_{HI} , on average, than EIG-1 galaxies (by a factor of 2.1 ± 0.6).

The actual average $\log (M_{HI}/M_\odot)$ of all EIGs of these subsamples are expected to be lower than the above values, since the EIGs not detected by ALFALFA are expected to have low M_{HI} values. However, adding the M_{HI} values of those EIGs is not expected to make the distributions of the EIG-1 and EIG-2 subsamples significantly more similar.

We can therefore conclude that extremely isolated galaxies that have neighbours with significant M_{HI} content at distances $< 3 h^{-1}$ Mpc tend to have higher M_{HI} compared to extremely isolated galaxies lacking such neighbours. The HI content of galaxies, therefore, seems to be environmentally dependent even in extremely isolated regions.

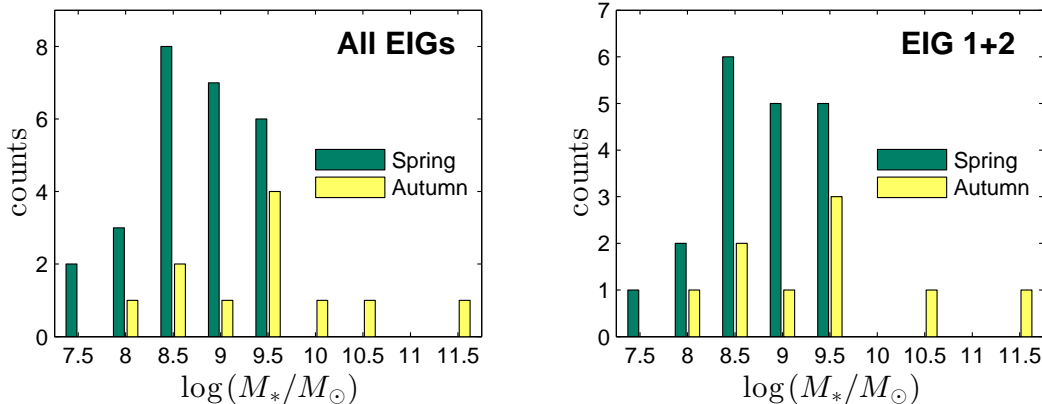


Figure 8. Stellar mass, M_* , histograms for Spring and Autumn EIGs. The left chart shows the histograms for all the EIGs. The right chart shows the histograms of subsamples EIG-1 and EIG-2.

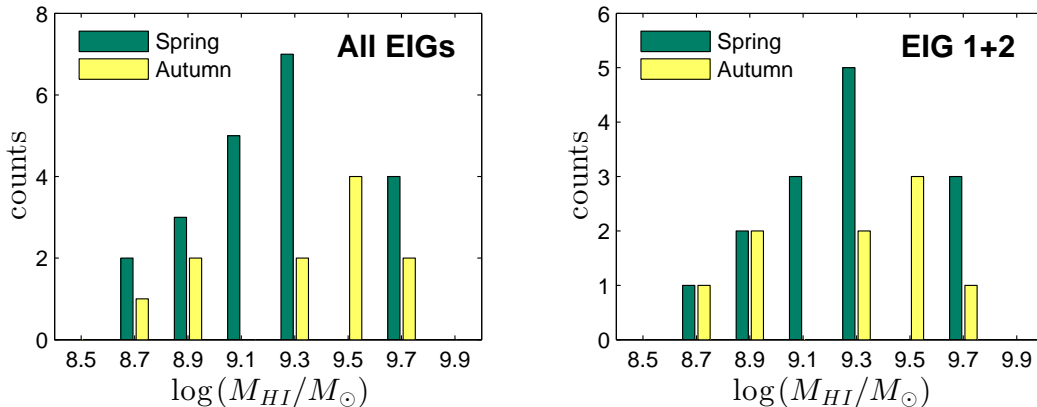


Figure 9. HI mass, M_{HI} , histograms for Spring and Autumn EIGs. The left chart shows the histograms for all the EIGs. The right chart shows the histograms of subsamples EIG-1 and EIG-2.

5.4 Scaling relations

The HI gas content can be combined with the SFR-to- M_* relation of Figure 7 in an attempt to investigate its connection to the main sequence of star-forming galaxies. This is done by breaking the SFR-to- M_* relation into a relation between the star formation and the HI gas content (Figure 14) and a relation between the HI content and M_* (Figure 15). Figure 14 shows SFR and star formation efficiency ($SFE \equiv SFR/M_{HI}$) vs. the HI mass, M_{HI} , of the EIGs. Figure 15 shows M_{HI} and $f_{HI} \equiv M_{HI}/M_*$ vs. the stellar mass, M_* , of the EIGs.

The average deviation of EIGs from the SFR-to- M_{HI} fit of Huang et al. (2012) is -0.04 ± 0.09 dex (with standard deviation of 0.5 dex). Despite the EIG's small range of $\log(M_{HI}/M_\odot)$ this indicates that the SFR-to- M_{HI} relation of EIGs is similar to that of the general population of star-forming galaxies.

The near-unity slope in the SFR-to- M_{HI} fit translates to a near-zero slope in SFE to M_{HI} (lower chart of Figure 14), implying that the SFE may be (statistically) independent of M_{HI} . To test this hypothesis, the Pearson product-moment correlation coefficient between SFE and M_{HI} of the EIGs was calculated. The resultant correlation coefficient,

-0.14 , is insignificant. If SFE and M_{HI} are not correlated, there is 0.52 chance of finding a correlation coefficient measurement at least this high. Therefore, the EIGs' measured data, supports independence of SFE and M_{HI} .

The following linear relation was fitted to the measured M_{HI} vs. M_* EIG points (marked by blue solid lines in Figure 15):

$$\log(M_{HI}/M_\odot) \cong 0.34 \cdot \log(M_*/M_\odot) + 6.20 \quad (11)$$

The expected standard deviation in $\log(M_{HI}/M_\odot)$ around this fit is marked in the figure by dashed blue lines (0.25 on average). The average $\log(M_{HI}/M_\odot)$ deviation of EIGs from the M_{HI} -to- M_* fit of Huang et al. (2012) is -0.16 ± 0.05 , implying that for a given stellar mass, M_* , the HI mass, M_{HI} , of EIGs is slightly lower, on average, than that of the general population of star-forming galaxies. However, some of this deviation may be a result of the difference between the M_* estimation method used by Huang et al. (2012) and the one used here.

Kudrya et al. (2011) analysed the M_{HI} -to- M_* relation for the 2MIG catalogue of isolated galaxies. The galaxies of the 2MIG catalogue have a range of M_* higher than that of the EIG sample (with the bulk in the range

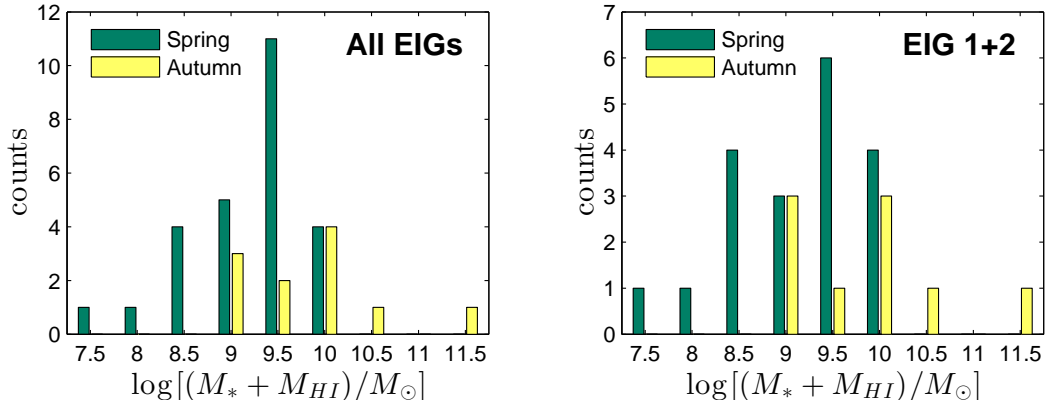


Figure 10. Stellar plus HI mass, $(M_* + M_{HI})$, histograms for Spring and Autumn EIGs. The left chart shows the histograms for all the EIGs. The right chart shows the histograms of subsamples EIG-1 and EIG-2.

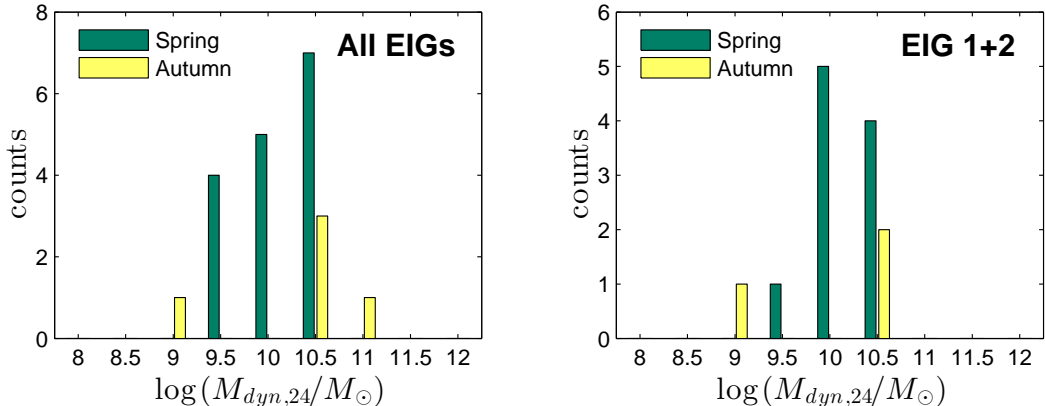


Figure 11. $M_{dyn,24}$ histograms for Spring and Autumn EIGs. The left chart shows the histograms for all the EIGs. The right chart shows the histograms of subsamples EIG-1 and EIG-2.

$9.5 < \log(M_*/M_\odot) < 11.5$). Most of these higher mass and less isolated galaxies have $M_{HI} < M_*$ (Kudrya et al. 2011, Fig. 10). This is in agreement with the results shown in Figure 15, where for $\log(M_*/M_\odot) > 9.5$ most galaxies have $\log(f_{HI}) < 0$. For their higher M_* sample Kudrya et al. (2011) found a slope (1.00 ± 0.04) in the linear fit of $\log(M_{HI}/M_\odot)$ as function of $\log(M_*/M_\odot)$ which is larger than the slope found here.

The following log-log predictor for SFR, using M_* and M_{HI} , was fitted to the EIGs data by a partial least-squares regression:

$$\log(\text{SFR}/M_\odot \text{ yr}^{-1}) \cong 0.580 \cdot \log(M_*/M_\odot) + 0.209 \cdot \log(M_{HI}/M_\odot) - 7.95 \quad (12)$$

The EIGs' SFRs are shown vs. this predictor in Figure 16. The expected standard deviation around this predictor is 0.29 dex (shown in the figure as dashed blue lines). It is somewhat lower than the 0.5 dex SFR-to- M_{HI} standard deviation around the Huang et al. (2012) relation, and the 0.4 dex standard deviation in the SFR to main sequence difference (Figure 7). Therefore, (12) that considers both M_* and M_{HI} is a more accurate estimate of SFR compared to

predictors based on M_* or on M_{HI} alone. It applies to EIGs, but is possibly also a good estimate for galaxies in denser regions that have not interacted with neighbours in the last few Gyr.

5.5 Morphology

It is evident from Table 4 that EIGs are typically late types (20 were classified as late-types, compared to six unknown and five early-types). Based on the 20 EIGs (65 per cent) that were classified as late-types, we conclude with 0.95 confidence that the probability for an EIG to be a late-type is ≥ 0.47 (using Wilson score interval for binomial distribution). Similarly, based on the five EIGs (16 per cent) classified as early-type we conclude with 0.95 confidence that the probability for an EIG to be an early-type is ≥ 0.07 . For comparison, Kreckel et al. (2012) identified three early-type galaxies (5 per cent) of the 60 isolated galaxies of the VGS sample. Sulentic et al. (2006) found in the most isolated subsample of AMIGA that 14 per cent are early-types (E-S0). Karachentsev et al. (2013) found that 5 per cent of the LOG sample galaxies are early-types (E-S0/a).

Of the five early-types, four are part of the EIG-1 subsample (galaxies that passed the isolation criterion using

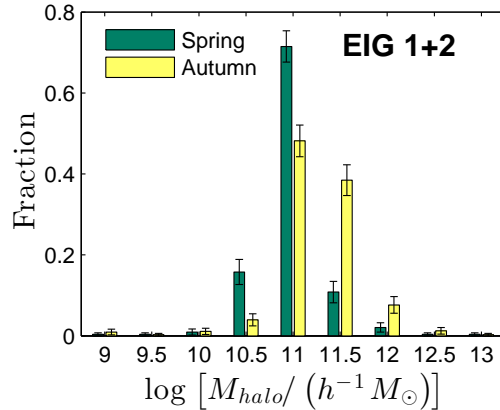


Figure 12. Simulation-based halo mass, M_{halo} , histogram calculated for the combination of subsamples EIG-1 and EIG-2. Adapted from Figure 6 of SB16.

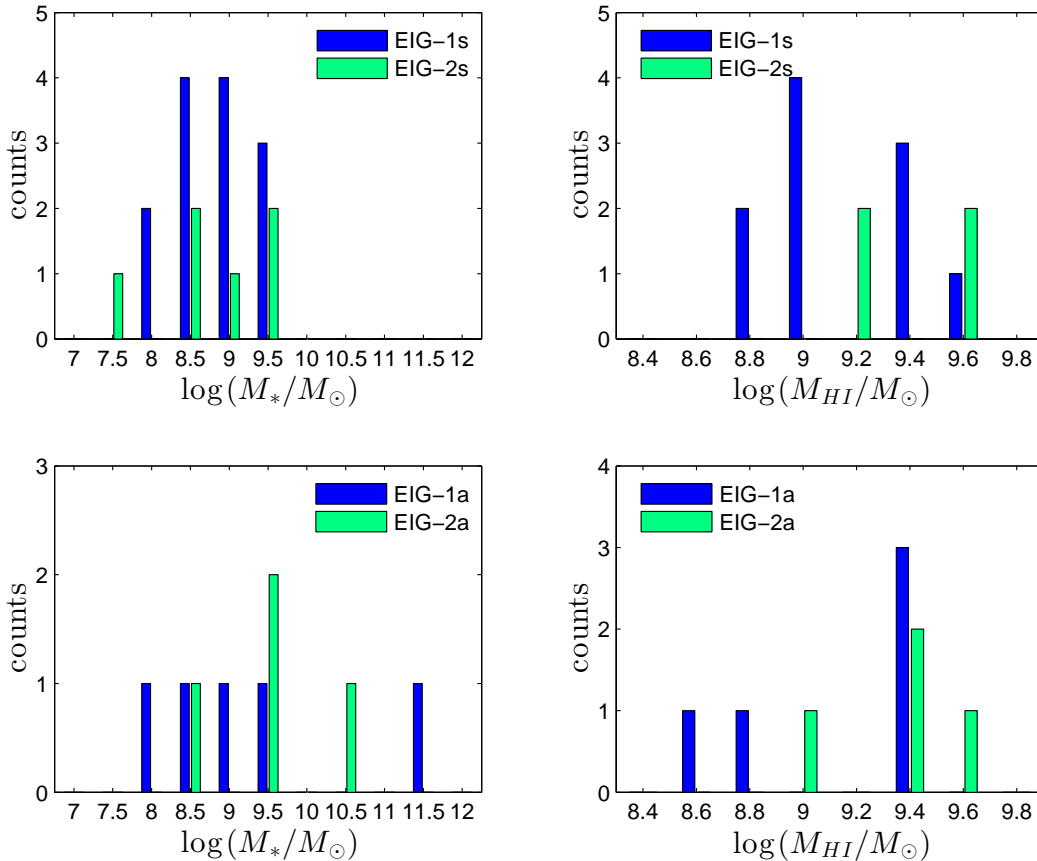


Figure 13. M_* (left charts), and M_{HI} (right charts) histograms comparing subsample EIG-1s with EIG-2s (upper charts) and EIG-1a with EIG-2a (lower charts). One EIG-1s galaxy, one EIG-2s galaxy and two EIG-1a galaxies are not included in the left charts, because they do not have M_* data. Four EIG-1s galaxies, three EIG-2s galaxies and two EIG-1a galaxies are not included in the right charts, because they were not detected by ALFALFA.

both NED and ALFALFA HI data as described in section 1). These make an early-type fraction significantly larger in the EIG-1 subsample (27 per cent) than in the entire EIG sample (16 per cent). The only early-type galaxy that is not part of the EIG-1 subsample, EIG 3s-01, passed the isolation criterion in the ALFALFA $\alpha.40$ dataset (but was slightly short of passing it in the NED dataset).

This means that none of the five early-type EIGs have ALFALFA (high HI content) neighbours within $3 h^{-1}$ Mpc. We can, therefore, conclude (with 0.94 confidence) that EIGs lacking high HI content neighbours within $3 h^{-1}$ Mpc have a higher tendency to be early-types, compared to EIGs that have such neighbours. As discussed in section 5.3, such EIGs with no high HI content neighbours tend to have a lower

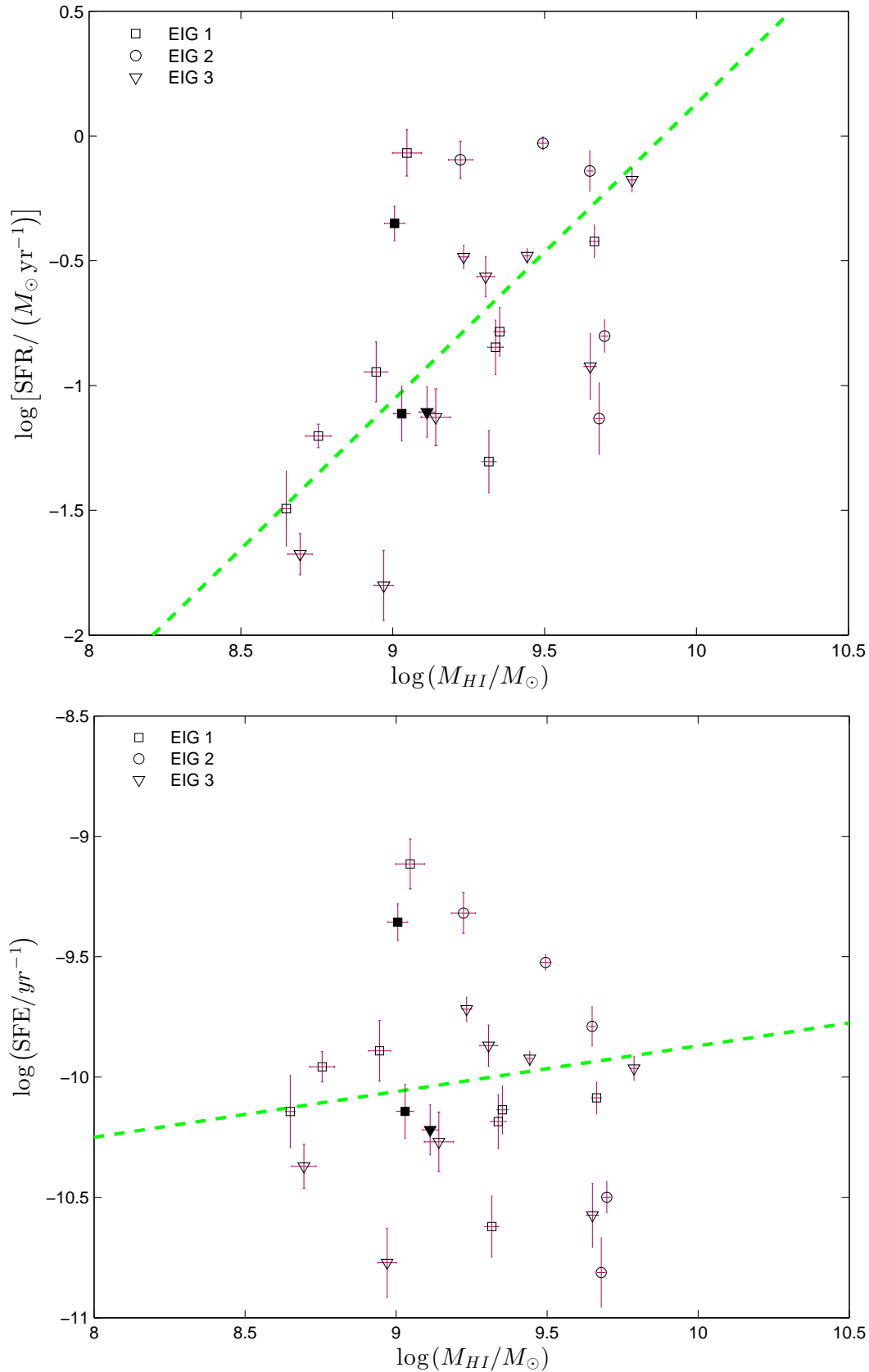


Figure 14. Star formation (SFR in the upper chart, and SFE in the lower chart) vs. HI mass, M_{HI} , of the EIGs. The green thick dashed lines show the fit found by (Huang et al. 2012, Fig. 4.b) for SFR to M_{HI} of star-forming ALFALFA galaxies. Filled symbols indicate EIGs classified as early-types.

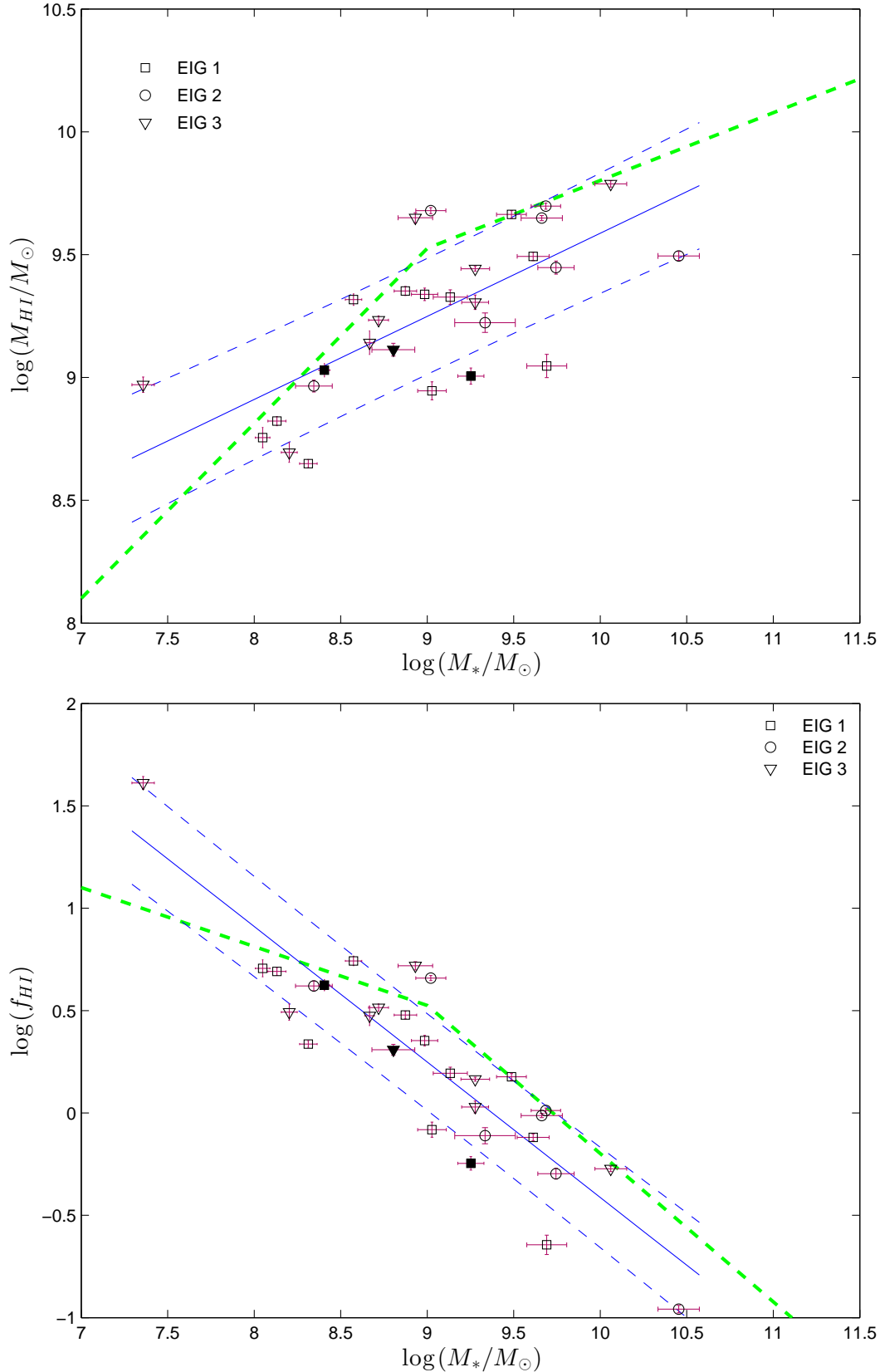


Figure 15. HI content (M_{HI} in the upper chart, and f_{HI} in the lower chart) vs. stellar mass, M_* , of the EIGs. The blue solid lines show a linear fit to the EIGs' M_{HI} to M_* data. The dashed blue lines show the $\pm 1\sigma$ deviation from this fit. The green thick dashed lines show the fit found by (Huang et al. 2012, eq. 1) for M_{HI} to M_* of star-forming ALFALFA galaxies. Filled symbols indicate EIGs classified as early-types.

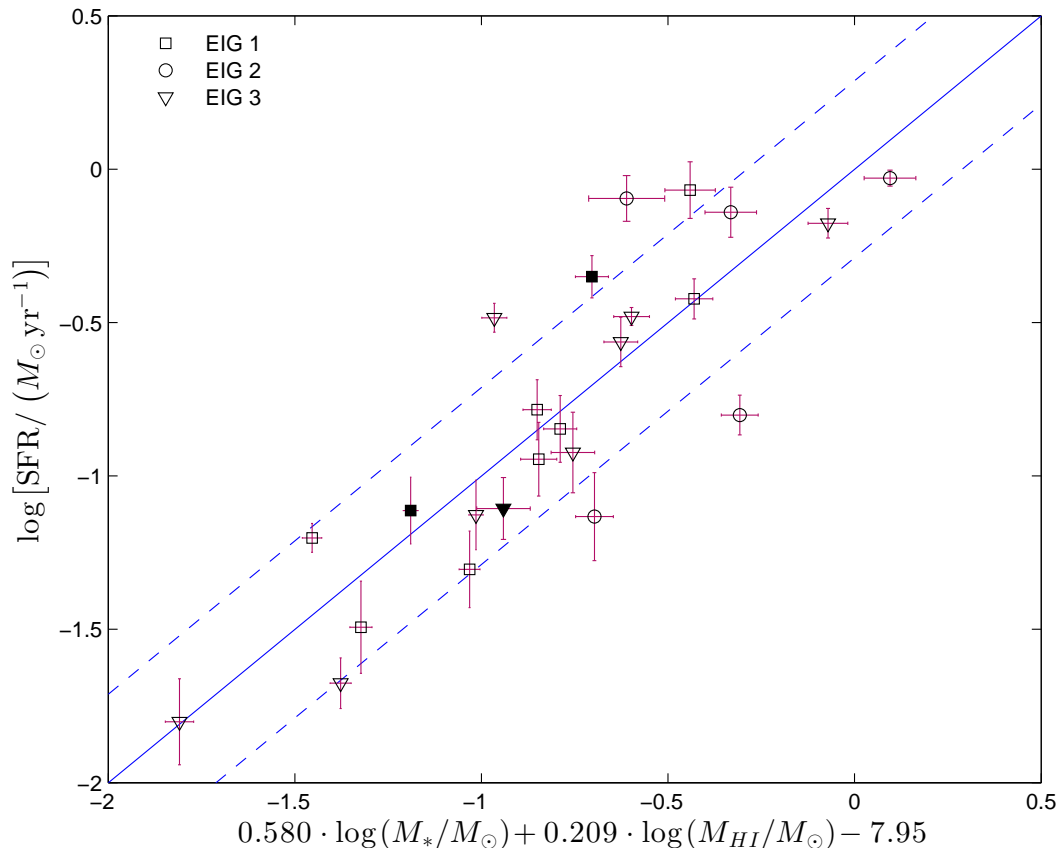


Figure 16. Star formation rate, SFR, vs. the M_* and M_{HI} partial least-squares regression predictor of (12). The blue solid line shows the one-to-one line. The dashed blue lines show the $\pm 1\sigma$ deviation from the one-to-one line. Filled symbols indicate EIGs classified as early-types.

HI content compared to ones with high HI content neighbours. This lower HI content may be linked to the fact that EIG-1 galaxies tend more to be early-types. From the EIG-1 subsample classification it can be concluded that for a galaxy that passes the strict isolation criterion of the EIG-1 subsample, the probability to be early-type is ≥ 0.11 (using Wilson score interval with 0.95 confidence).

Only one of the early-types, EIG 1a-04, is not classified as blue in Figure 5 but is rather a ‘green valley’ galaxy. Three others (1s-02, 1s-12 and 3s-01) are blue, and the colour classification of the last, EIG 3s-01, is unknown. This means that an extremely isolated early-type galaxy has a probability ≥ 0.30 of being blue (with 0.95 confidence). This may be compared to the 0.057 ± 0.004 fraction of blue galaxies found by Schawinski et al. (2009) in the low-redshift early-type galaxy population, and to the ~ 0.20 fraction of blue galaxies found by Lacerna et al. (2016) in their sample of isolated early-types.

All five early-type EIGs are within 0.5 dex of the main sequence in Figure 7. From this we conclude that an extremely isolated early-type galaxy has a probability ≥ 0.57 (with 0.95 confidence) of fitting the main sequence of star-forming galaxies to within 0.5 dex.

A large fraction of the EIGs show asymmetric star formation, and many show strong compact star-forming regions

(see Figures 1, 2 and 3 and Tables 9 and 10). This indicates that star formation is a stochastic process that may occur unevenly across a galaxy in a given time, even in the most isolated galaxies. Sources of the randomness of star formation may include uneven ‘fuelling’ of gas, and collisions with very small satellites (e.g., with $M_{halo} < 10^9 h^{-1} M_\odot$) that could not be detected around the EIGs studied here.

6 DISCUSSION AND CONCLUSIONS

We have found surprising environmental dependencies of the HI content, M_{HI} , and of the morphological type of EIGs (sections 5.3 and 5.5 respectively). It is generally accepted that galaxies in cluster environments typically have atomic gas deficiencies (Kennicutt 1998), while void galaxies are typically gas-rich (Cortese et al. 2011; Kreckel et al. 2012; Lacerna et al. 2014). It is also generally accepted that early-type galaxies are more abundant in clusters than in isolated environments (Bamford et al. 2009). It was, therefore, expected that a sample of the most isolated galaxies (subsample EIG-1) would be the most gas-rich and would contain the lowest fraction of early-types.

However, contrary to these expectations, we have found that EIG-1 galaxies, which lack neighbours with significant M_{HI} content at distances $< 3 h^{-1}$ Mpc, tend to have lower M_{HI} compared to EIG-2 galaxies that have such neighbours

(the average M_{HI} of EIG-1 galaxies is lower than that of EIG-2 galaxies with 2.5σ confidence). Moorman et al. (2014) have found a similar M_{HI} environmental dependence, in which their sample of void galaxies showed a tendency for lower M_{HI} compared to their sample of wall galaxies.

Similarly unexpected, we have found that the most isolated galaxies (subsample EIG-1) have a higher tendency to be early-types compared to EIG-2 galaxies (with 0.94 confidence). To the best of our knowledge this is the first time where an isolated galaxies' sample shows a higher fraction of early-types compared to a less isolated sample.

These findings do not contradict the results of Cortese et al. (2011); Kreckel et al. (2012); Lacerna et al. (2014) and Bamford et al. (2009) which compared isolated galaxies with galaxies in clusters or with the general population of galaxies. Here we compared between two galaxy populations of extreme isolation levels, and showed that the trends of increased M_{HI} and decreased early-type fraction with the increase of the isolation level reverse at extreme isolation (or when the isolation is tested also with respect to the M_{HI} of possible neighbours).

There is considerable evidence from cosmological simulations that the spins and major axes of haloes are correlated with the direction of the walls or filaments in which they reside (e.g., Aragón-Calvo et al. 2007; Zhang et al. 2009; Codis et al. 2012; Libeskind et al. 2014). For low-mass haloes ($\log [M_{halo}/(h^{-1} M_{\odot})] < 13$ according to Zhang et al. 2009, or $\log [M_{halo}/(h^{-1} M_{\odot})] < 12.6$ according to Codis et al. 2012), the halo spin is more likely to be aligned with the closest filament. This preferred spin direction is probably a result of the direction from which material is accreted to the halo. As shown in Figure 12, simulation analysis indicates that almost all EIGs reside in haloes that would be considered low-mass in this respect, and are, therefore, expected to have spins that correlate fairly well with the direction of the filaments and walls closest to them.

We speculate that this effect may be connected to the low abundance of early-types in the EIG-2 subsample and to its higher average M_{HI} compared to the EIG-1 subsample. Underdense filaments and walls may be the hosts of EIG-2 galaxies. The halo spins induced by their filament or wall environment may significantly reduce their early-type fraction and possibly also increase their M_{HI} (because the gas may spend more time before reaching their centres). If they indeed reside in filaments or walls, they are also expected to have some neighbours with similar tendency for being late-type and containing significant amounts of M_{HI} .

We further speculate that a significant fraction of EIG-1 galaxies are not parts of filaments or walls, but rather reside in environments with no preferred direction for accreting material (e.g., at the junction points between filaments so extremely underdense that no galaxies were detected in them). This may increase their probability of being early-types and may also affect them in such a way that they would contain less HI on average (either because there is not much gas in their environment or because the available HI gas is accreted faster to the halo's centre and forms stars more quickly). Further study of the early-type EIGs found in this work may be of interest, since if they indeed reside at junction points between filaments, they may resemble cluster early-types at early stages of their development.

Both the early-type and late-type EIGs follow the same colour-to- M_* relation (Fig. 5), SFR-to- M_* 'main sequence' relation (Fig. 7) and M_{HI} -to- M_* relation (Fig. 15), and fit the SFR predictor of eq. (12) (Fig. 16). This indicates that the mechanisms and factors governing star formation, colour and the M_{HI} -to- M_* relation are similar in early-type and late-type EIGs. It further indicates that the morphological type of EIGs is not governed by their M_{HI} content, SFR or colour. EIGs with high M_{HI} content, high SFR or blue colour are not necessarily late-types.

Our observations indicate that EIGs typically fit the 'main sequence of star forming galaxies' found by Huang et al. (2012). This indicates that the extreme isolation of the EIGs does not affect their SFR considerably compared to field galaxies. This is supported by Beygu et al. (2016) who found no significant difference in SF between void galaxies of the VGS sample and field galaxies.

We have found that EIGs follow a colour-to- M_* relation, in which EIGs with M_* smaller than $10^{(10.6 \pm 0.9)} M_{\odot}$ are typically 'blue cloud' galaxies irrespective of their morphological type (Figure 5). Since M_* of most EIGs is below this threshold, most of the EIGs are blue. A similar result was found by Bamford et al. (2009) who found that in low density environments low M_* galaxies are mostly blue, while galaxies with high M_* are mostly red (irrespective of morphology). This is contrary to what is found in high density environments, where galaxies are mostly red irrespective of their M_* and morphology.

With respect to the 'Nature vs. Nurture' question, which was the primary driver of this work, we conclude the following: It is well known that cluster environments have a strong effect on star formation, colours and morphologies of galaxies. With the exception of these high density environments the SFR is not significantly affected by the environment, i.e. the 'main sequence of star-forming galaxies' holds in a range of environments from walls to the most extremely isolated regions measurable. Outside high density regions, the colours of galaxies are mostly related to their stellar mass, M_* , and are less affected (if at all) by the environment.

We have found that the HI content, M_{HI} , and the morphological type of galaxies do depend on their environment. In the most isolated environments, where no neighbours with significant M_{HI} are present (to a distance of $3h^{-1}$ Mpc), galaxies tend more to be early-types and have lower M_{HI} , on average, compared to less isolated environments. We speculate that this might reflect the large scale structure of these extremely isolated regions. Late-type and high- M_{HI} galaxies may be more abundant in underdense filaments and walls, while early-type and lower M_{HI} galaxies may be more abundant at the junctions of filaments so extremely underdense that no galaxies were detected in them.

ACKNOWLEDGEMENTS

We are grateful to Martha Haynes, Riccardo Giovanelli and the entire ALFALFA team for providing an unequalled HI data set.

This research has made use of the NASA/IPAC Extragalactic Database (NED) which is operated by the Jet Propulsion Laboratory, California Institute of Technology, under contract with the National Aeronautics and Space Administration. Funding for SDSS-III has been provided by the Alfred P. Sloan Foundation, the Participating Institutions, the National Science Foundation, and the U.S. Department of Energy Office of Science. The SDSS-III web site is <http://www.sdss3.org/>.

This research has made use of observations made with the NASA Galaxy Evolution Explorer. GALEX is operated for NASA by the California Institute of Technology under NASA contract NAS5-98034. This research has also made use of the NASA/IPAC Infrared Science Archive (IRSA), which is operated by the Jet Propulsion Laboratory, California Institute of Technology, under contract with the National Aeronautics and Space Administration. This publication makes use of data products from the Two Micron All Sky Survey (2MASS), which is a joint project of the University of Massachusetts and the Infrared Processing and Analysis Center/California Institute of Technology, funded by the National Aeronautics and Space Administration and the National Science Foundation. This publication makes use of data products from the Wide-field Infrared Survey Explorer (WISE), which is a joint project of the University of California, Los Angeles, and the Jet Propulsion Laboratory/California Institute of Technology, funded by the National Aeronautics and Space Administration.

REFERENCES

- Acquaviva V., Gawiser E., Guaita L., 2011a, in *The Spectral Energy Distribution of Galaxies Vol. 7 of Proceedings of the International Astronomical Union*, Sed fitting with mcmc: methodology and application to large galaxy surveys. pp 42–45
- Acquaviva V., Gawiser E., Guaita L., 2011b, *ApJ*, 737, 47
- Ahn C. P., Alexandroff R., Allende Prieto C., Anders F., Anderson S. F., Anderton T., Andrews B. H., Aubourg É., et al. 2014, *ApJS*, 211, 17
- Almoznino E., 1995, PhD thesis, Tel Aviv University
- Almoznino E., Brosch N., 1998, *MNRAS*, 298, 920
- Aragón-Calvo M. A., van de Weygaert R., Jones B. J. T., van der Hulst J. M., 2007, *ApJ*, 655, L5
- Argudo-Fernández M., Verley S., Bergond G., Duarte Pueras S., Ramos Carmona E., Sabater J., Fernández Lorenzo M., Espada D., Sulentic J., Ruiz J. E., Leon S., 2015, *A&A*, 578, A110
- Baldry I. K., Balogh M. L., Bower R. G., Glazebrook K., Nichol R. C., Bamford S. P., Budavari T., 2006, *MNRAS*, 373, 469
- Bamford S. P., Nichol R. C., Baldry I. K., Land K., Lintott C. J., Schawinski K., Slosar A., Szalay A. S., Thomas D., Torki M., Andreescu D., Edmondson E. M., Miller C. J., Murray P., Raddick M. J., Vandenberg J., 2009, *MNRAS*, 393, 1324
- Behroozi P. S., Wechsler R. H., Conroy C., 2013, *ApJ*, 770, 57
- Bennett C. L., Hill R. S., Hinshaw G., Larson D., Smith K. M., Dunkley J., Gold B., Halpern M., et al. 2011, *ApJS*, 192, 17
- Bergvall N., Laurikainen E., Aalto S., 2003, *A&A*, 405, 31
- Beygu B., Kreckel K., van der Hulst J. M., Jarrett T. H., Peletier R., van de Weygaert R., van Gorkom J. H., Aragon-Calvo M. A., 2016, preprint (arXiv:1601.08228)
- Binggeli B., Popescu C. C., Tammann G. A., 1993, *A&AS*, 98, 275
- Blanton M. R., Roweis S., 2007, *AJ*, 133, 734
- Bouché N., Dekel A., Genzel R., Genel S., Cresci G., Förster Schreiber N. M., Shapiro K. L., Davies R. I., Tacconi L., 2010, *ApJ*, 718, 1001
- Brosch N., 1983, PhD thesis, Rijksuniversiteit Leiden, 142 p.
- Brosch N., Almoznino E., Spector O., Zitrin A., 2008, in *1st Middle-East African Regional IAU Meeting Star Formation in Various Environments*
- Brosch N., Bar-Or C., Malka D., 2006, *MNRAS*, 368, 864
- Brosch N., Heller A., Almoznino E., 1998, *ApJ*, 504, 720
- Brosch N., Isaacman R., 1982, *A&A*, 113, 231
- Brosch N., Shaviv G., 1982, *ApJ*, 253, 526
- Calzetti D., Armus L., Bohlin R. C., Kinney A. L., Koornneef J., Storchi-Bergmann T., 2000, *ApJ*, 533, 682
- Calzetti D., Kinney A. L., Storchi-Bergmann T., 1994, *ApJ*, 429, 582
- Codis S., Pichon C., Devriendt J., Slyz A., Pogosyan D., Dubois Y., Sousbie T., 2012, *MNRAS*, 427, 3320
- Cohen M., Wheaton W. A., Megeath S. T., 2003, *AJ*, 126, 1090
- Conroy C., Wechsler R. H., 2009, *ApJ*, 696, 620
- Cortese L., Catinella B., Boissier S., Boselli A., Heinis S., 2011, *MNRAS*, 415, 1797
- Courteau S., Cappellari M., de Jong R. S., Dutton A. A., Emsellem E., Hoekstra H., Koopmans L. V. E., Mamon G. A., et al. 2014, *Reviews of Modern Physics*, 86, 47
- Croton D. J., Farrar G. R., 2008, *MNRAS*, 386, 2285
- Croton D. J., Farrar G. R., Norberg P., Colless M., Peacock J. A., Baldry I. K., Baugh C. M., Bland-Hawthorn J., et al. 2005, *MNRAS*, 356, 1155
- Cutri R. M., Wright E. L., Conrow T., Fowler J. W., Eisenhardt P. R. M., Grillmair C., Kirkpatrick J. D., Masci F., et al. 2013, Technical report, Explanatory Supplement to the AllWISE Data Release Products
- Deng X.-F., Song J., Chen Y.-Q., Jiang P., Ding Y.-P., 2012, *ApJ*, 753, 166
- Dressler A., 1980, *ApJ*, 236, 351
- Durkalec A., Le Fèvre O., de la Torre S., Pollo A., Cassata P., Garilli B., Le Brun V., Lemaux B. C., Maccagni D., et al. 2015, *A&A*, 576, L7
- Fernández Lorenzo M., Sulentic J., Verdes-Montenegro L., Argudo-Fernández M., 2013, *MNRAS*, 434, 325
- Fernández Lorenzo M., Sulentic J., Verdes-Montenegro L., Blasco-Herrera J., Argudo-Fernández M., Garrido J., Ramírez-Moreta P., Ruiz J. E., et al. 2014, *ApJ*, 788, L39
- Fernández Lorenzo M., Sulentic J., Verdes-Montenegro L., Ruiz J. E., Sabater J., Sánchez S., 2012, *A&A*, 540, A47
- Gavazzi G., Jaffe W., 1985, *ApJ*, 294, L89
- Giovanelli R., Haynes M. P., Kent B. R., Perillat P., Sain-tonge A., Brosch N., Catinella B., Hoffman G. L., et al. 2005, *AJ*, 130, 2598
- Giovanelli R., Haynes M. P., Kent B. R., Saintonge A., Stierwalt S., Altaf A., Balonek T., Brosch N., et al. 2007, *AJ*, 133, 2569
- Grogin N. A., Geller M. J., 1999, *AJ*, 118, 2561

- Guo Q., White S., Angulo R. E., Henriques B., Lemson G., Boylan-Kolchin M., Thomas P., Short C., 2013, *MNRAS*, 428, 1351
- Hall M., Courteau S., Dutton A. A., McDonald M., Zhu Y., 2012, *MNRAS*, 425, 2741
- Hao C.-N., Kennicutt R. C., Johnson B. D., Calzetti D., Dale D. A., Moustakas J., 2011, *ApJ*, 741, 124
- Haynes M. P., Giovanelli R., Martin A. M., Hess K. M., Saintonge A., Adams E. A. K., Hallenbeck G., Hoffman G. L., et al. 2011, *AJ*, 142, 170
- Heller A. B., 2001, PhD thesis, Tel Aviv University
- Hernández-Toledo H. M., Vázquez-Mata J. A., Martínez-Vázquez L. A., Choi Y.-Y., Park C., 2010, *AJ*, 139, 2525
- Hoffman G. L., Glosson J., Helou G., Salpeter E. E., Sandage A., 1987, *ApJS*, 63, 247
- Huang S., Haynes M. P., Giovanelli R., Brinchmann J., 2012, *ApJ*, 756, 113
- Jester S., Schneider D. P., Richards G. T., Green R. F., Schmidt M., Hall P. B., Strauss M. A., Vanden Berk D. E., et al. 2005, *AJ*, 130, 873
- Karachentsev I. D., Karachentseva V. E., Melnyk O. V., Courtois H. M., 2013, *Astrophysical Bulletin*, 68, 243
- Karachentsev I. D., Makarov D. I., Karachentseva V. E., Melnyk O. V., 2011, *Astrophysical Bulletin*, 66, 1
- Karachentseva V. E., Mitronova S. N., Melnyk O. V., Karachentsev I. D., 2010, *Astrophysical Bulletin*, 65, 1
- Kennicutt R. C., Evans N. J., 2012, *ARA&A*, 50, 531
- Kennicutt Jr. R. C., 1998, *ARA&A*, 36, 189
- Kreckel K., Platen E., Aragón-Calvo M. A., van Gorkom J. H., van de Weygaert R., van der Hulst J. M., Beygu B., 2012, *AJ*, 144, 16
- Kudrya Y. N., Karachentseva V. E., Karachentsev I. D., 2011, *Astrophysics*, 54, 445
- Lacerna I., Hernández-Toledo H. M., Avila-Reese V., Abonza-Sane J., del Olmo A., 2016, *A&A*, 588, A79
- Lacerna I., Rodríguez-Puebla A., Avila-Reese V., Hernández-Toledo H. M., 2014, *ApJ*, 788, 29
- Lambas D. G., Maddox S. J., Loveday J., 1992, *MNRAS*, 258, 404
- Landolt A. U., 1992, *AJ*, 104, 340
- Lee K.-S., Ferguson H. C., Wiklund T., Dahlen T., Dickinson M. E., Gialalisco M., Grogan N., Papovich C., et al. 2012, *ApJ*, 752, 66
- Lewis A., Bridle S., 2002, *Phys. Rev. D*, 66, 103511
- Libeskind N. I., Knebe A., Hoffman Y., Gottlöber S., 2014, *MNRAS*, 443, 1274
- Lilly S. J., Carollo C. M., Pipino A., Renzini A., Peng Y., 2013, *ApJ*, 772, 119
- Madau P., 1995, *ApJ*, 441, 18
- Martin D. C., Fanson J., Schiminovich D., Morrissey P., Friedman P. G., Barlow T. A., Conrow T., Grange R., et al. 2005, *ApJ*, 619, L1
- Matthee J., Schaye J., Crain R. A., Schaller M., Bower R., Theuns T., 2017, *MNRAS*, 465, 2381
- McClure M., 2009, *ApJ*, 693, L81
- Melnyk O., Mitronova S., Karachentseva V., 2014, *MNRAS*, 438, 548
- Moorman C. M., Moreno J., White A., Vogeley M. S., Hoyle F., Giovanelli R., Haynes M. P., 2016, preprint (arXiv:1601.04092)
- Moorman C. M., Vogeley M. S., Hoyle F., Pan D. C., Haynes M. P., Giovanelli R., 2014, *MNRAS*, 444, 3559
- Mould J. R., Huchra J. P., Freedman W. L., Kennicutt Jr. R. C., Ferrarese L., Ford H. C., Gibson B. K., Graham J. A., et al. 2000, *ApJ*, 529, 786
- Murphy E. J., Condon J. J., Schinnerer E., Kennicutt R. C., Calzetti D., Armus L., Helou G., Turner J. L., et al. 2011, *ApJ*, 737, 67
- Noeske K. G., Weiner B. J., Faber S. M., Papovich C., Koo D. C., Somerville R. S., Bundy K., Conselice C. J., et al. 2007, *ApJ*, 660, L43
- Oke J. B., 1990, *AJ*, 99, 1621
- Pustilnik S. A., Martin J.-M., Huchtmeier W. K., Brosch N., Lipovetsky V. A., Richter G. M., 2002, *A&A*, 389, 405
- Rieke G. H., Alonso-Herrero A., Weiner B. J., Pérez-González P. G., Blaylock M., Donley J. L., Marcillac D., 2009, *ApJ*, 692, 556
- Rodríguez-Puebla A., Avila-Reese V., Yang X., Foucaud S., Drory N., Jing Y. P., 2015, *ApJ*, 799, 130
- Rojas R. R., Vogeley M. S., Hoyle F., Brinchmann J., 2004, *ApJ*, 617, 50
- Rojas R. R., Vogeley M. S., Hoyle F., Brinchmann J., 2005, *ApJ*, 624, 571
- Saintonge A., 2007, *AJ*, 133, 2087
- Salim S., Rich R. M., Charlot S., Brinchmann J., Johnson B. D., Schiminovich D., Seibert M., Mallery R., et al. 2007, *ApJS*, 173, 267
- Schaerer D., de Barros S., 2009, *A&A*, 502, 423
- Schaerer D., Vacca W. D., 1998, *ApJ*, 497, 618
- Schawinski K., Lintott C., Thomas D., Sarzi M., Andreescu D., Bamford S. P., Kaviraj S., Khochfar S., et al. 2009, *MNRAS*, 396, 818
- Schawinski K., Urry C. M., Simmons B. D., Fortson L., Kaviraj S., Keel W. C., Lintott C. J., Masters K. L., et al. 2014, *MNRAS*, 440, 889
- Schlafly E. F., Finkbeiner D. P., 2011, *ApJ*, 737, 103
- Skrutskie M. F., Cutri R. M., Stiening R., Weinberg M. D., Schneider S., Carpenter J. M., Beichman C., Capps R., et al. 2006, *AJ*, 131, 1163
- Sorrentino G., Rifatto A., Antonuccio-Delogu V., 2006, in *Galaxy Evolution Across the Hubble Time Vol. 2 of Proceedings of the International Astronomical Union, Galaxy properties from voids to clusters in the sdss-dr4*. pp 243–243
- Spector O., 2015, PhD thesis, Tel Aviv University, <http://primage.tau.ac.il/libraries/theses/exeng/free/-2842601.pdf>
- Spector O., Brosch N., 2016, *MNRAS*, 456, 885
- Spector O., Finkelman I., Brosch N., 2012, *MNRAS*, 419, 2156
- Strateva I., Ivezić Ž., Knapp G. R., Narayanan V. K., Strauss M. A., Gunn J. E., Lupton R. H., Schlegel D., et al. 2001, *AJ*, 122, 1861
- Sulentic J. W., Verdes-Montenegro L., Bergond G., Lisenfeld U., Durbala A., Espada D., Garcia E., Leon S., Sabater J., Verley S., Casanova V., Sota A., 2006, *A&A*, 449, 937
- Tinker J. L., Conroy C., 2009, *ApJ*, 691, 633
- Varela J., Moles M., Márquez I., Galletta G., Masegosa J., Bettoni D., 2004, *A&A*, 420, 873
- Verley S., Leon S., Verdes-Montenegro L., Combes F., Sabater J., Sulentic J., Bergond G., Espada D., et al. 2007, *A&A*, 472, 121
- Wang W., White S. D. M., 2012, *MNRAS*, 424, 2574

Wen X.-Q., Wu H., Zhu Y.-N., Lam M. I., Wu C.-J., Wicker J., Long R. J., Zhao Y.-H., 2014, MNRAS, 438, 97
 Wright E. L., Eisenhardt P. R. M., Mainzer A. K., Ressler M. E., Cutri R. M., Jarrett T., Kirkpatrick J. D., Padgett D., et al. 2010, AJ, 140, 1868
 Yuan H. B., Liu X. W., Xiang M. S., 2013, MNRAS, 430, 2188
 Zhang Y., Yang X., Faltenbacher A., Springel V., Lin W., Wang H., 2009, ApJ, 706, 747
 Zitrin A., Brosch N., 2008, MNRAS, 390, 408

APPENDIX A: EIG SPECIFIC DATA

This appendix contains general notes for some of the EIGs.

EIG 1s-05

No optical counterpart could be identified for EIG 1s-05 (an ALFALFA object). In the Wise Observatory images, no H_α emission was identified around the ALFALFA coordinates. Within one arcminute from the ALFALFA coordinates of EIG 1s-05, all galaxies detected by SDSS have $g > 21.6$, and none have spectroscopic redshifts. All GALEX detected objects in the same region have $m_{FUV} > 24$ and $m_{NUV} > 21$. EIG 1s-05 may, therefore, be a ‘dark galaxy’ with an extremely high HI to stellar mass ratio and a very low SFR. It may also be an ALFALFA false detection, even though its SNR is 8.1 and it is considered a ‘code 1’ object, i.e. a source of SNR and general qualities that make it a reliable detection (Haynes et al. 2011).

EIG 1s-09

SDSS DR10 shows an edge-on galaxy, SDSS J112157.63+102959.6, $\sim 13''$ east of the centre of EIG 1s-09. The angular size of SDSS J112157.63+102959.6 is similar to that of EIG 1s-09. Its magnitude is $g = 18.6$, compared to $g = 16.9$ of EIG 1s-09. The redshift of SDSS J112157.63+102959.6 is unknown. Although there is a possibility that SDSS J112157.63+102959.6 is a close neighbour of EIG 1s-09, this seems unreasonable, since tidal tails are neither visible in the SDSS images nor in the images shown in figure 1 (which combine 40 minute exposure in the R band and 120 minute exposure in an H_α band, both using the WO 1 meter telescope).

EIG 1s-10

SDSS DR10 shows two objects at an angular distance of $\sim 6''$ from the centre of EIG 1s-10. One is north of EIG 1s-10, and is classified as a star by SDSS DR10. The second, classified as a galaxy, is south-west of EIG 1s-10. Both objects do not have measured redshifts. Although there is a possibility that one or both of these are galaxies merging with EIG 1s-10, this seems unreasonable, since tidal tails are neither visible in the SDSS images nor in the images shown in figure 1 (which combine 100 minute exposure in the R band and 260 minute exposure in an H_α band, both using the WO 1 meter telescope).

EIG 1s-11

The only redshift measurement found for EIG 1s-11 is from Binggeli et al. (1993) that quotes Hoffman et al. (1987). This is a HI measurement made at the Arecibo observatory. The HI-profile for the galaxy was not published by Hoffman et al. (1987). It is possible that the measurement ($4725 \pm 10 \text{ km s}^{-1}$) is a result of HI-confusion, and that EIG 1s-11 is actually a part of the Virgo cluster.

EIG 1s-14

EIG 1s-14 is projected close to a bright foreground star, which prevented SDSS from measuring its spectrum. This also affected the accuracy of measurement of its magnitudes and H_α flux here. Its relative H_α flux uncertainty was 0.3. Its estimated uncertainty in *ugriz* was 0.1 mag.

EIG 1a-02

SDSS DR10 shows a galaxy, SDSS J005629.17+241913.3, $\sim 2'$ west of EIG 1a-02 with unknown redshift. The angular size of SDSS J005629.17+241913.3 is not very different from that of EIG 1a-02. Its magnitude is $g = 16.6$, compared to $g = 17.0$ of EIG 1a-02. Although there is a possibility that SDSS J005629.17+241913.3 is a close neighbour of EIG 1a-02, this is probably not the case, since no tidal tails or other signs of interaction are visible in the SDSS images. However, since EIG 1a-02 was not imaged using the WO 1 meter telescope we cannot be certain of this, as tidal tails and other fine structure features are hard to see or detect in shallow images like those of SDSS.

EIG 1a-04

H_α images of EIG 1a-04 showed strong star formation in LEDA 213033, a galaxy separated by $107''$ from EIG 1a-04. Since LEDA 213033 has no measured redshift, its distance from EIG 1a-04 is unknown. The fact that it shows emission in the two narrow H_α filters used for the measurement, indicates that its redshift is $cz \cong 6000 \pm 1500 \text{ km s}^{-1}$. Therefore, the probability that it is less than 300 km s^{-1} away from EIG 1a-04 is estimated to be ~ 0.1 . No sign of interaction between EIG 1a-04 and LEDA 213033 was detected.

EIG 2s-04

The H_α flux of EIG 2s-04 could not be measured due to a foreground star ($r = 14.30$) at a projected distance of $12''$. Although EIG 2s-04 has a GALEX measurement (in NUV only) it was not used, since it is contaminated with flux from this foreground star.

EIG 2s-06

A foreground star of magnitude $r = 15.6$, which is comparable to that of EIG 2s-06, is projected close to the EIG’s centre. Its presence interfered with the photometric measurements, somewhat reducing the measured flux. The SDSS automatic photometry of EIG 2s-06 did not produce reliable results; the EIG was identified as two galaxies separated

by the foreground star. GALEX measurements for this EIG were not used, since they also are contaminated by the foreground star. The morphological type of EIG 2s-06 was not classified because of the foreground star.

EIG 3s-06

This is the only EIG that passes the isolation criterion using the ALFALFA dataset, but had neighbours closer than $3 h^{-1}$ Mpc in the NED dataset. It was classified as part of subsample EIG-3s, because all of its NED neighbours are more than $2 h^{-1}$ Mpc away from it.

APPENDIX B: MODELLED EIG PROPERTIES

The SFH, dust attenuation and stellar mass of the EIGs were estimated by fitting a model to their UV-to-near-IR SEDs as described section 4.3. Figure B1 shows, for each of the modelled EIGs, the marginalized posterior distributions of Age_1 , τ^{-1} , $E(B - V)$, M_2 and M_* . The extreme τ^{-1} values where $|\tau| \ll Age_1$ represent scenarios in which the first stellar population was created in a short burst. The low τ^{-1} values (where $|\tau| \gg Age_1$) represent an almost constant star formation for the first (main) stellar population.

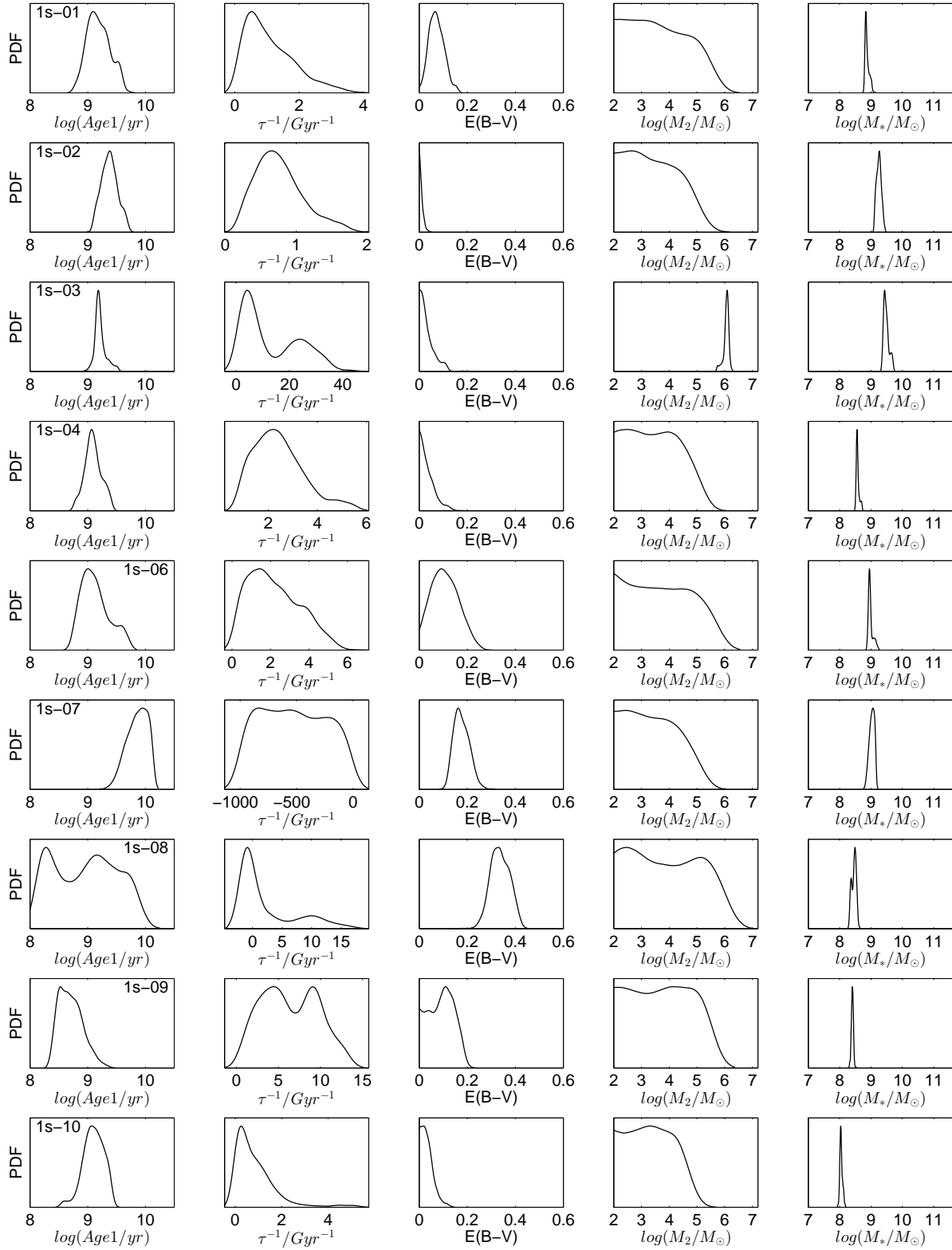


Figure B1. Modelled one-dimensional marginalized posterior distributions of Age_1 , τ^{-1} , $E(B-V)$, M_2 and M_* . Data for each EIG is plotted in a separate row.

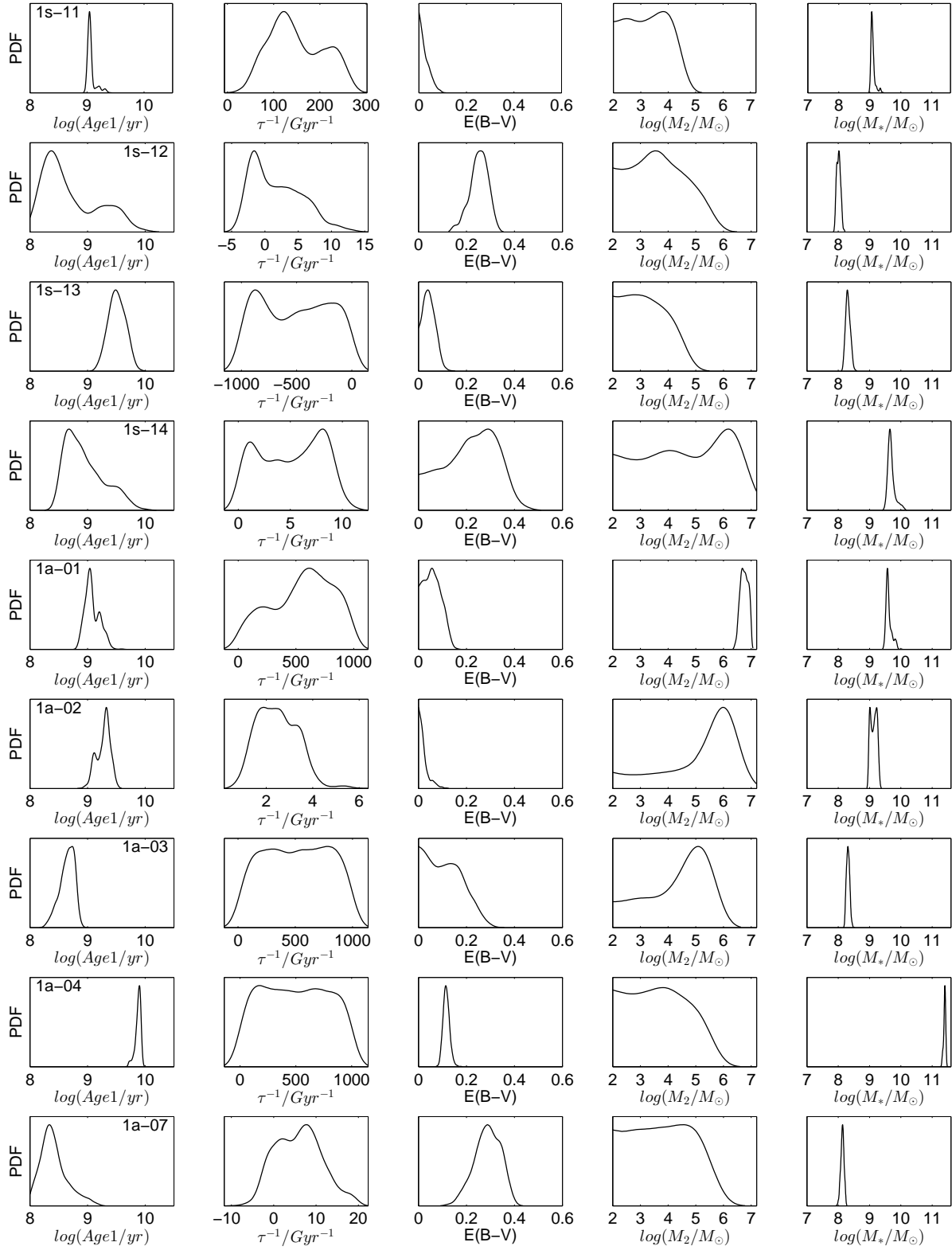


Figure B1 – continued

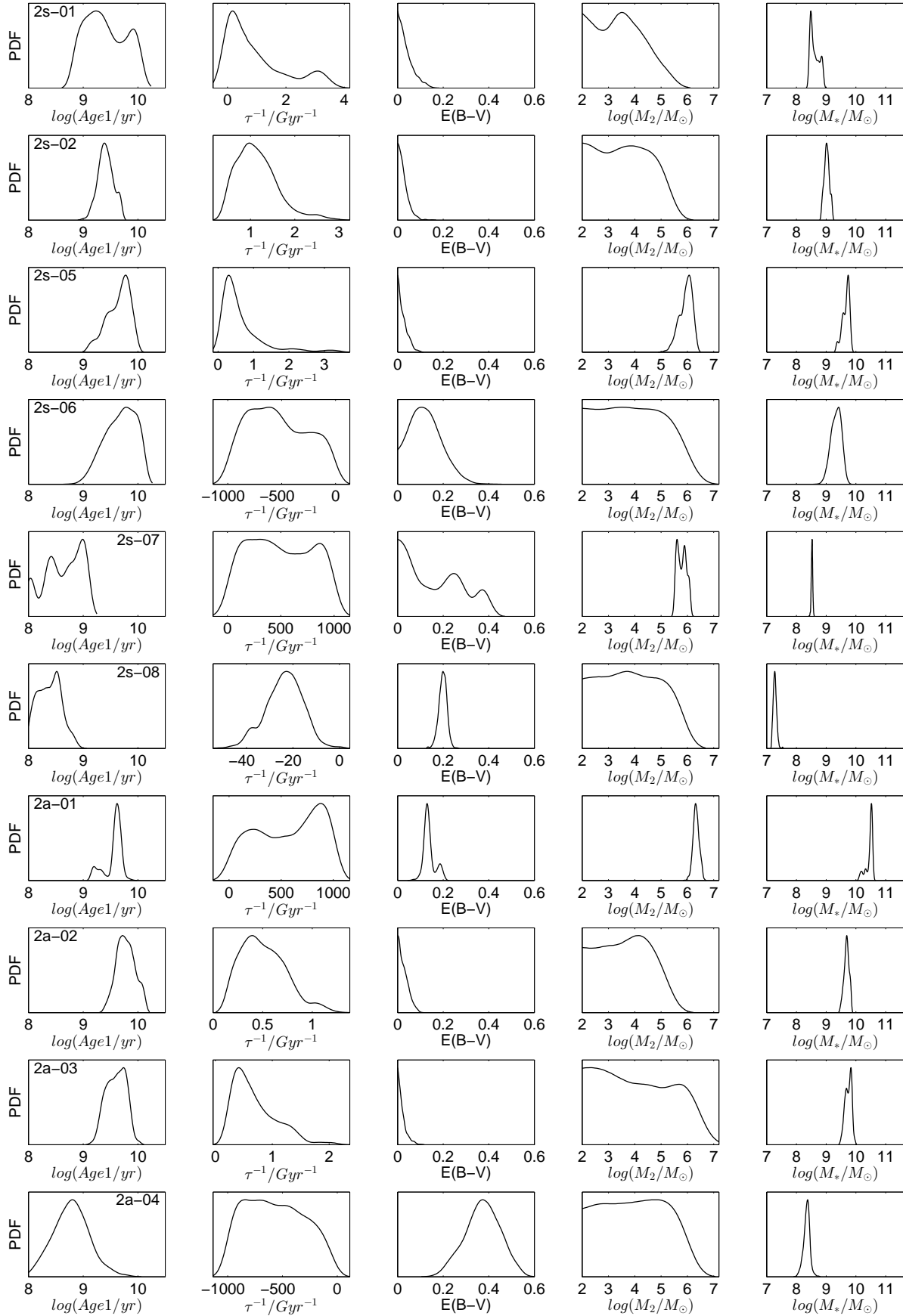


Figure B1 – continued

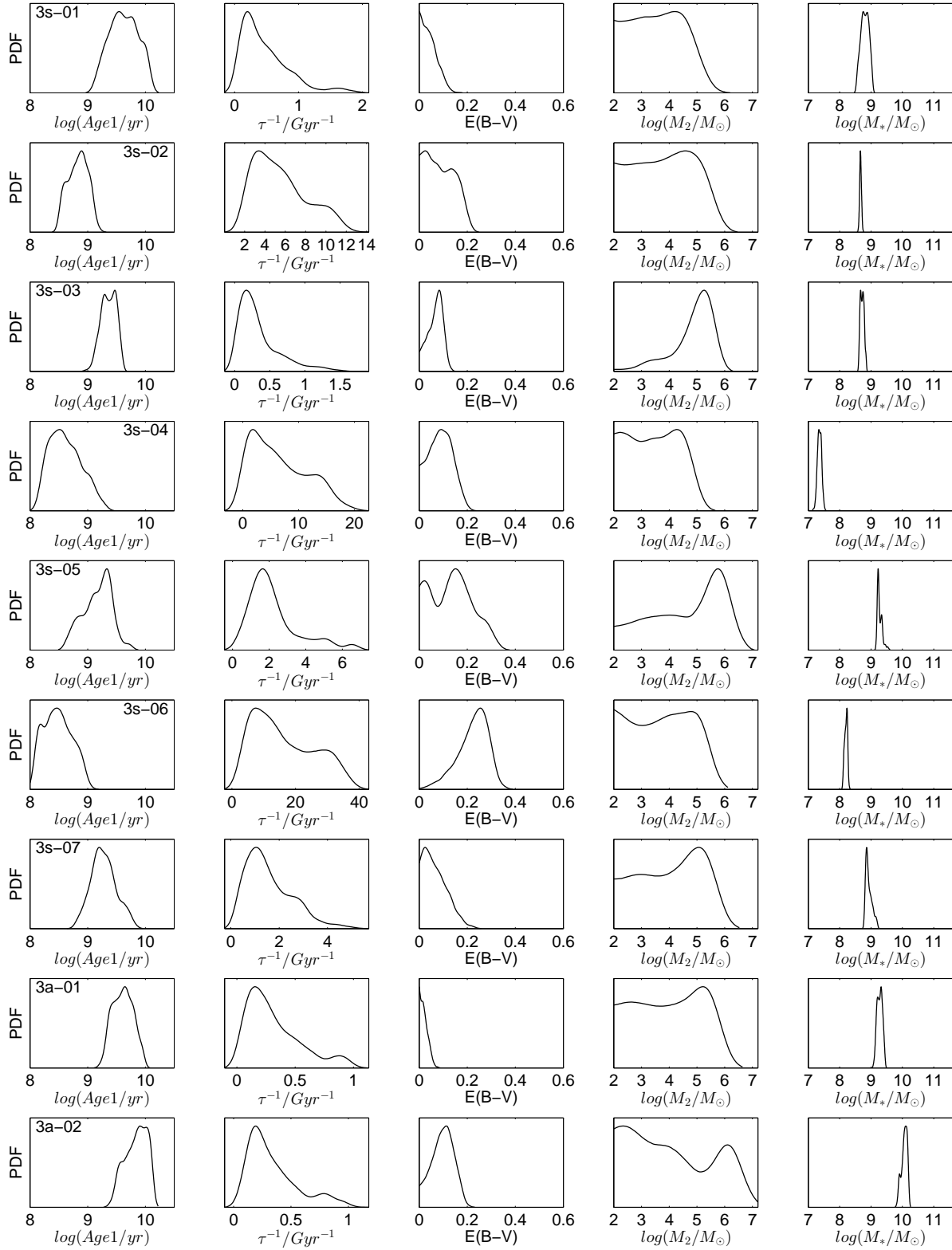


Figure B1 – continued